Available online at www.sciencedirect.com

ScienceDirect

Physics of Life Reviews 43 (2022) 98–138

PHYSICS of LIFE reviews

www.elsevier.com/locate/plrev

Review

‘Phase transitions’ in bacteria – From structural transitions in free living bacteria to phenotypic transitions in bacteria within biofilms

Xiaoling Wang [a,b,*], Raphael Blumenfeld [c], Xi-Qiao Feng [d], David A. Weitz [b,e]

[a] *School of Mechanical Engineering, University of Science and Technology Beijing, Beijing 100083, China*
[b] *John A. Paulson School of Engineering and Applied Sciences, Harvard University, 9 Oxford St, Cambridge, MA, 02138, USA*
[c] *Gonville & Caius College, University of Cambridge, Trinity St., Cambridge CB2 1TA, UK*
[d] *Institute of Biomechanics and Medical Engineering, Department of Engineering Mechanics, Tsinghua University, Beijing 100084, China*
[e] *Department of Physics, Harvard University, 9 Oxford St, Cambridge, MA, 02138, USA*

Received 28 September 2022; accepted 30 September 2022
Available online 5 October 2022
Communicated by M. Frank-Kamenetskii

Abstract

Phase transitions are common in inanimate systems and have been studied extensively in natural sciences. Less explored are the rich transitions that take place at the micro- and nano-scales in biological systems. In conventional phase transitions, large-scale properties of the media change discontinuously in response to continuous changes in external conditions. Such changes play a significant role in the dynamic behaviours of organisms. In this review, we focus on some transitions in both free-living and biofilms of bacteria. Particular attention is paid to the transitions in the flagellar motors and filaments of free-living bacteria, in cellular gene expression during the biofilm growth, in the biofilm morphology transitions during biofilm expansion, and in the cell motion pattern transitions during the biofilm formation. We analyse the dynamic characteristics and biophysical mechanisms of these phase transition phenomena and point out the parallels between these transitions and conventional phase transitions. We also discuss the applications of some theoretical and numerical methods, established for conventional phase transitions in inanimate systems, in bacterial biofilms.

Keywords: Phase transitions in bacteria; Flagellar structure; Biofilm; Phenotype; Morphology

1. Introduction

1.1. Phase and phase transitions

Phase transition phenomena have been studied for over a century [1–4]. In inanimate systems, a phase transition is characterised by the appearance, or disappearance, of order on small, sometimes molecular, scales. Traditional examples are the transitions from gas to liquid and solid with decreasing temperature, corresponding to the appearances of

* Corresponding author.
E-mail address: xiaoling@me.ustb.edu.cn (X. Wang).

https://doi.org/10.1016/j.plrev.2022.09.004
1571-0645/

order in the spatial correlation functions. Other examples include the occurrence of directional correlations in magnetic systems and liquid crystals and the structural change of graphite into diamond under pressure. Phase transitions often lead to changes in macroscopic properties, such as viscosity in the gas-to-liquid transition, elastic moduli in the liquid-to-solid transition, magnetisation in the paramagnetic-to-ferromagnetic transition, and optical properties in the thermotropic-to-nematic transition in liquid crystals. In these examples, the order emerging at the molecular scale corresponds to a structural symmetry or invariance. However, the smallest scale may be sometimes much larger, such as in suspensions of interacting colloids, which can be either disordered or ordered, depending on its density. We will refer to the smallest scale in such systems as the micro-scale even though it may in fact be much larger than microns. Such a micro-structural spatial rearrangement may result in changes in the macroscopic physical properties.

Recent research in biophysics raises a pertinent question: can the concept of phase transition be extended to characterise, understand, and model biological systems? If yes, this could lead to progress on a number of important issues, including how do phase transition phenomena arise in living organisms, what roles they play in the life process, the dynamic mechanisms driving them, their macro-scale effect and purpose, etc. These issues are important because most biological systems rely on a specific internal structure, into which they self-organise to perform specific functions. Self-organisation is, by definition, generation of structures of specific order, albeit not always the simple symmetry-based orders that occur in inanimate matter. Straightforward examples are the functions of all the different systems in the human body, from cell sorting during embryo formation to tissue self-organisation [5–8]. These spatial structures can change in response to external stimuli, modifying functionality and behaviour. Examples abound in nature: pulling a B-DNA by 70 pN transforms its structure into an S-DNA, which is twice as long and of different functionality [9–14]. Torsion transforms DNA from a denatured state to a P-DNA structure, which interacts better with some proteins [9]. Stretching proteins causes a transition from folded to unfolded states, which inspired the design of better glues [9–14]. By injecting its own DNA into *Escherichia coli* (*E. Coli*), the virus bacteriophage T4 changes its tail sheath structure [15–19].

The parallels between such transitions and conventional phase transitions suggest that insight gained from the latter and traditional methods from physics may be applied to biological systems. However, this raises further questions. Most biological systems can transition into a functional state from another state (whether functional or not), each of which having its own order and structure. This means that there is a huge number of possible structural states. Can each such state be regarded as a distinct phase? If yes, then the transition from a disordered, or disorganised state, to an ordered functional one is a phase transition. But, if so, how can one apply insight from traditional phase transitions to understand or characterise better biological systems? If the answer is no, then why not and what exactly distinguishes transitions in self-organising biological systems from traditional phase transitions? Can some such transitions be regarded as phase transitions while others cannot?

Many traditional phase transitions occur in what is known as Hamiltonian systems, in which energy and thermodynamic potentials are well defined. In such systems, the phases are *equilibrium* states, which are minima in the thermodynamic potentials. These potentials are functions of macroscopic variables, such as temperature, pressure, density, and external fields. A typical example of such potentials, the Helmholtz free energy, is sketched in Fig. 1, as a function of one variable, say, the density ϕ of the system. The two minima represent two distinct phases of different energies, and a circle represents the state of the system. Raising the temperature, for example, increases the effect of entropy and reduces the barrier between the phases, until at some critical temperature, the system makes a transition from phase A (on the left on the red curve) to phase B (on the right on the black curve).

Non-Hamiltonian inanimate systems also display a wide range of transitions and processes, through processes of self-organisation into non-random static structures or steady states with unique characteristics [8]. Such states can also be classified and characterised usefully by phase diagrams and, in some limited cases, can be even described by models similar to conventional statistical mechanics [20–22].

In contrast, biological systems are active and inherently out of thermal equilibrium. In this sense, they resemble many self-organising, out-of-equilibrium inanimate systems. However, the main difference lies in their ability to convert external resources into energy that drives essential processes. Given external resources and stimuli, most biological systems can settle into a normal steady-state operation mode. Active matter, including both biological and non-biological systems that are able to convert external resources into motion, can also settle into a rich variety of steady states. Many works in the literature on these out-of-equilibrium systems have used successfully the concept of phase transformations [15,23–25].

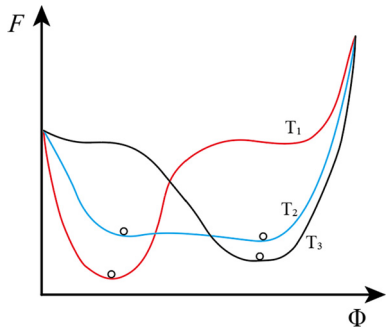

Fig. 1. Changing the order parameter modifies the free energy. Changing the temperature modifies the free energy, F, plotted as a function of an order parameter, Φ. The modification of the free energy causes a transition of the system (represented as small circles) from phase A (red curve, T_1), first into a mixture A-B phases (blue curve, T_2) and then to phase B (black curve, T_3). The order parameter could be pressure, density, magnetisation, etc.

In this review, we will address the above questions related to phase transitions in living bacterial organisms, including structural transitions in both bacterial flagellar filaments and flagellar motors. These transitions allow a cell to switch between the motions of swimming and tumbling. We also describe the transitions that occur in the formation of bacterial biofilms, including phenotypic transitions, morphological transitions, and cell motion pattern evolutions in *Bacillus Subtilis* (*B. Subtilis*) biofilms. We discuss how these transitions proceed and affect the bacterial behaviour. The similarities and differences between these and traditional phase transitions will be analysed. Finally, we propose ways to gain insight into biological transitions by using tools developed for phase transitions and self-organisation in inanimate systems.

1.2. Bacterium and its flagella

Bacteria are one of the first life forms that appeared on Earth. Measuring a few microns in size, these one-cell organisms come in a variety of shapes, including spheres, rods, and spirals. Flagella, first observed by Ehrenberg in 1838, is a typical structure that drives the locomotion of bacteria [26]. Flagella are membrane-embedded filamentous organelles, which the bacteria rotate to drive themselves in aqueous environments or over semi-solid media. The energy required to generate the flagellar rotation comes from the electrochemical gradient between the cell membrane due to flux of protons and ions. The rotation itself is generated by a motor at the base of the flagellum, which is helically shaped and, therefore, acts as a propeller. The flagellum consists of three major substructures: **the filament**, **the hook** (a flexible coupling universal joint), and **the basal body** (consisting of a reversible rotary motor embedded in the cell wall). The filament is a hollow tube, 20 nm in diameter and 15 – 20 μm long, which usually consists of thousands of copies of a single protein called flagellin, as shown in Fig. 2 [27–30].

We focus here on the types of bacteria whose motion is driven by flagella. A flagellum is shaped as a left-handed helix that, when rotating counter-clockwise (CCW), propels the cell through the fluid. When one or more flagella separate from the flagellar bundle and change conformation to form a right-handed helix [31], as shown in Fig. 3, the bacterium stops 'swimming' and tumbles. This transition is induced by the flagellar motors embedded in the cell wall and the cytoplasmic membrane. The motors act similarly to man-made ones, with the rotation driven by protons or ions crossing the cellular membrane. Bacterial swimming is possible when all the motors rotate in the CCW direction, while tumbling takes place when one or more motors start rotating in the clockwise (CW) direction.

1.3. Biofilm

The number of bacteria in the world is staggering. For example, a typical gram of soil contains 40 million bacteria and a millilitre of fresh water normally contains about a million bacterial cells. These group together for better survival and more than 99% of bacteria in the natural world live in biofilm communities. This way they can fight better other cells and survive environmental threats.

B. *Subtilis* bacteria can be either free-living individually or part of a biofilm attached to a surface. Free-living bacteria, also known as planktonic, can attach either reversibly or irreversibly to a surface [32]. The latter involves

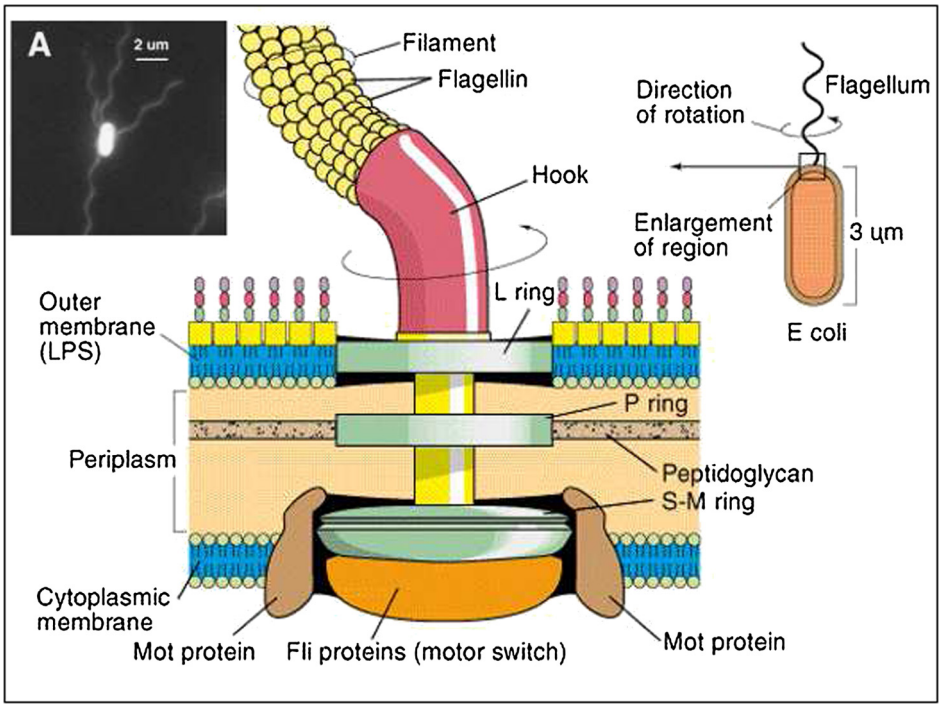

Fig. 2. A functional sketch of the flagellar structure. Inset A: an immobilised cell of *E. Coli* from [31].

strengthening of bacteria-surface adhesion and production of extracellular polymeric substances (EPS), composed primarily of polysaccharides [33] and proteins [34,35]. The EPS forms the scaffolding for the biofilm, supporting its mechanical integrity. The biofilm life cycle comes a full circle when a biofilm disperses with individual bacteria leaving [36,37], as illustrated in Fig. 4. Biofilm-based bacteria exhibit surprisingly intricate social behaviour patterns, both cooperative and competitive, made possible by their sophisticated genetic networks and cell biology. To facilitate this, the biofilm's organisation is driven by complex physical, chemical, and biological mechanisms. Consequently, to fully understand the properties of biofilms requires an interdisciplinary approach, integrating microbiology with physics, mechanics, materials science, and chemistry. In the following, we use tools borrowed from physics to discuss transitions and phase transition phenomena in both free-living and biofilm-based bacterial cells, as well as how these phenomena shape bacterial behaviours.

2. Phase transition phenomena

2.1. Non-equilibrium phase transition in the flagellar motor switching between CCW and CW rotations

Rotary motors, which are ubiquitous in man-made machinery, also exist in biological systems. Only flagellated bacteria are known to incorporate this mechanism in their locomotive strategy. Their motion is driven by rotary bacterial flagellar motors that spin long filaments, which sprout from the cell body [38–42]. Bacterial flagellar motors are distributed across the cellular surface, each comprising several transmembrane rings that connect to the bacterium's flagellar filament by a flexible hook. These rings are approximately 45 nm in diameter and contain about 25 different proteins, shown in Figs. 5a and b. The flagellar motors of *E. Coli* and *Salmonella*, which consist of a rotor and a dozen stator units, is powered by an electrochemical potential of protons across the cytoplasmic membrane, known as a proton motive force [43]. Marine *Vibrio* and extremely alkalophilic *Bacillus* utilise instead sodium motive force as the energy source to drive flagellar motor rotation, shown schematically in Fig. 5c.

The motors can rotate either CCW or CW and they alternate between the two. Experiments [52] have shown that regulation of the flagellar motor rotation direction is inherent to the three flagella-driven motility species: *Salmonela*, *B. Subtilis*, and *E. Coli*. The regulation is achieved by modifying the cellular metabolism, which changes the proton-

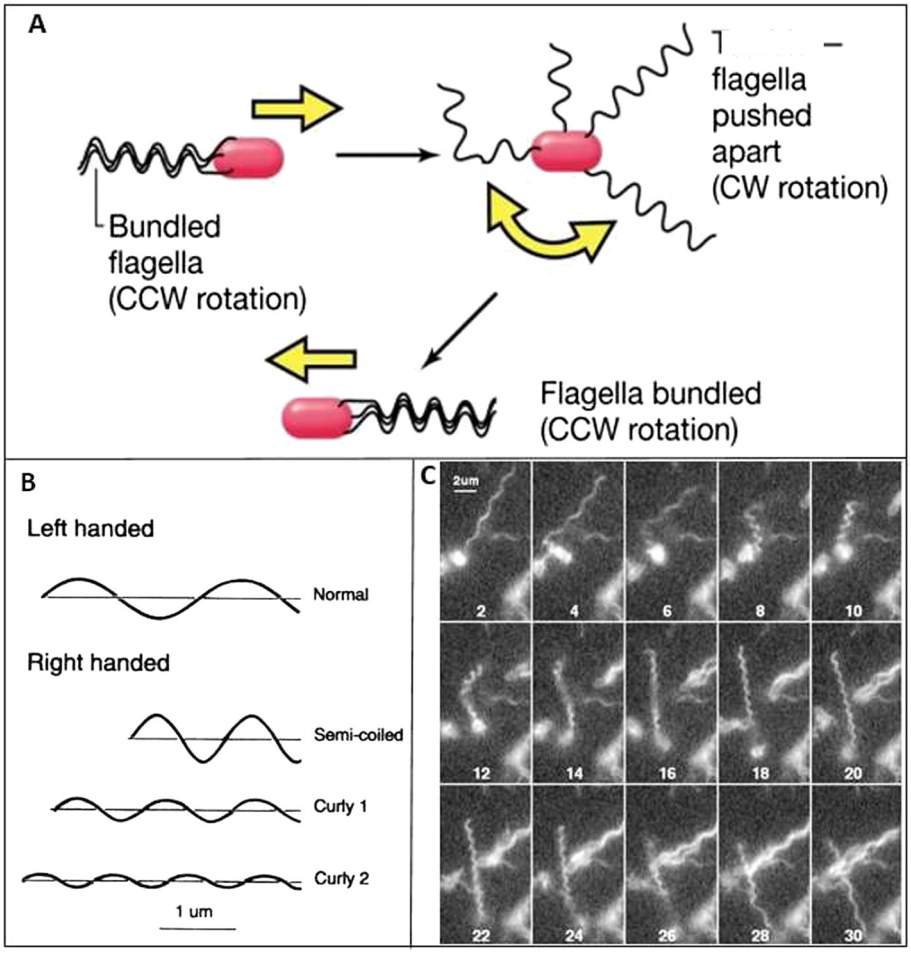

Fig. 3. The flagellar structure controls bacterial motion and can undergo a transition. A. When all the helical filaments rotate in the CCW direction, the cell is propelled through a fluid; this is the 'run' phase. When one or more filaments rotate clockwise the cell's motion halts and it reorients; this is the 'tumble' phase. During the tumble phase, the filament undergoes a polymorphic transition. B. Four waveforms of a 4 μm long filament (adapted from [11]). Such a filament has ∼8,000 flagellin molecules [17]. The normal filament (top sketch) is left-handed, while the semi-coiled, curly 1, and curly 2 filaments (shown below) are right-handed. C. *E. Coli* cell, with one flagellar filament, undergoing a polymorphic transformation. B and C are from [31].

or ion-motive potential, and is independent of the viscosity load, i.e., the resistance to rotation [52]. The higher the motor rotation speed the longer the flagella rotate in the CW direction. The motility threshold in *B. Subtilis* is about 30 mV and the threshold for switching rotation direction is about 45 mV. By measuring the relative durations of the CW and CCW states as a function of motor speed, an analogue of a thermal-equilibrium two-state activation diagram has been constructed in [52], reproduced in Fig. 6. Specifically, reducing the protonmotive force reduces the motor speed, ϕ, which leads to lowering of the barrier for the CW $\rightarrow$ CCW transition. This lowering can be interpreted as the Arrhenius law for the rate of chemical reactions. This measurement made possible to estimate the changes in the relative state free energies, $\delta F_{CW}(\phi)$ and $\delta F_{CCW}(\phi)$, as functions of the motor speed and the exponential increase of the activation rate as it changes from ϕ to ϕ-$\delta\phi$ [52,53] (see Fig. 6). The signalling regulating the motor speed was shown to a signalling protein, CheY-P, with lower levels of CheY-P promoting CCW rotation and vice versa [54–57].

A recent study [58] found two different molecular architectures of the flagellar motors in *B. Burgdorferi* during CCW and CW rotations, which are triggered by the protein CheY3-P binding, as shown in Fig. 7. In the absence of bound CheY3-P, the FliG2 proteins, which are protein components in the C-ring, interact with the inner part of the stator complex, which gives rise to the CCW state. CheY3-P induces conformational changes in the C-ring, resulting in altered interactions between the stator and the C-ring, causing in turn a switch to CW rotation. The CheY3-P

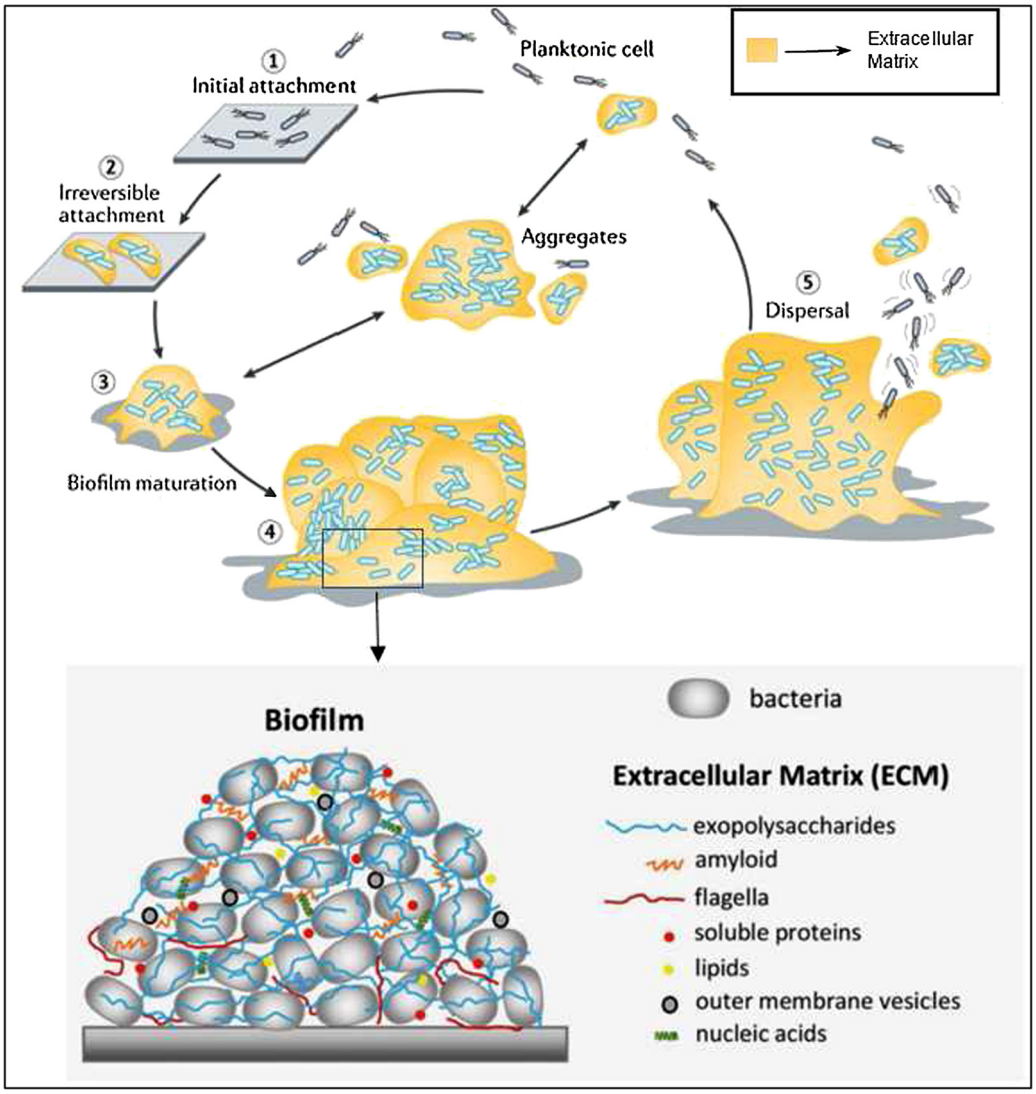

Fig. 4. The biofilm life cycle. A sketch of the cyclic process that is the formation of biofilms of single-species *Pseudomonas aeruginosa* biofilms [36,37]. The stages of the process are distinct and ordered. In Step 1, as single planktonic cells come into contact with the surface, they attach reversibly either via the cell pole or the flagellum. In Step 2, the cells are cemented to the surface irreversibly and nascent clusters form. This is accompanied by loss of flagellum gene expression and production of biofilm matrix components. Step 3: the biofilm matures into thickness of several layers, embedded in an extracellular matrix. Step 4: the biofilms reach maximum thickness and are mature. Step 5: the biofilm disperses, and the cycle reverts to the origin.

protein interacts directly with the FliM protein, which is part of the C-ring, thereby inducing a major remodelling of the switch protein FliG2. The back-and-forth conformational changes of FliG2 cause the switch complex to interact with opposite sides of the rotating torque generator and it is this interaction that facilitates the switch between CW and CCW rotations, as sketched in Fig. 8.

In most conventional models, the switch is regarded as an equilibrium of a two-state system (Fig. 6), with the PMF driving a conformational change in the motor by changing the concentration of the binding CheY-P. In turn, this changes the free energies of the two states [52,59,60]. Similar thermal-equilibrium models include the classical Monod–Wyman–Changeux allosteric model [61–63] and the two-state Ising model [64] with nearest-neighbour interactions. Korobkova et al. [65] found that the CW and CCW intervals could be described by a gamma distribution, suggesting the existence of hidden Markov steps preceding each motor switch, which indicates a non-equilibrium switching process of the bacterial motor, as well as in other large cooperative molecular systems. Tu proposed a

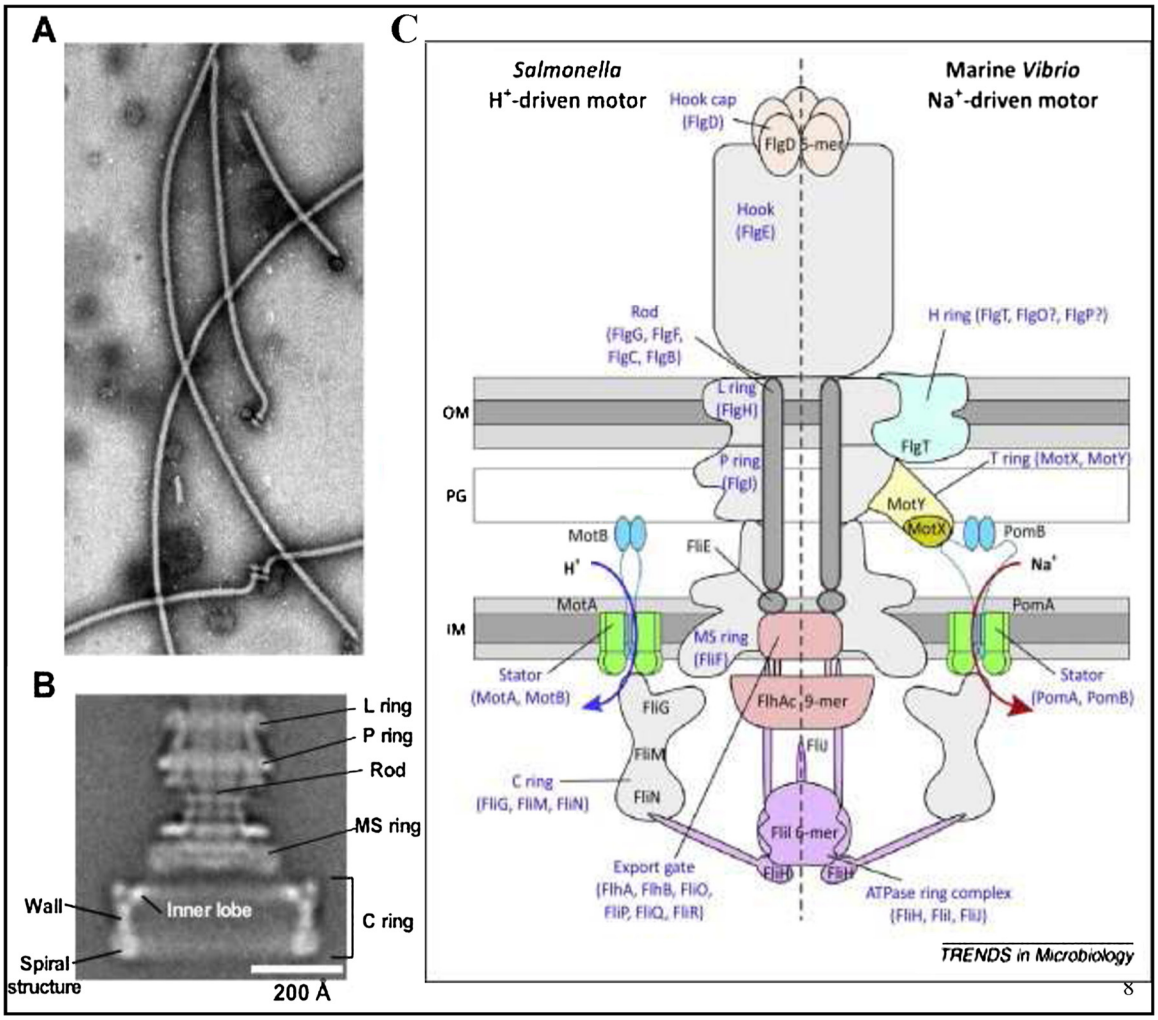

Fig. 5. Organisation of the flagellar motor. **A.** Electron micrograph of flagella purified from *Salmonella*. The flagellum consists of a basal body acting as a rotary motor, a hook acting as a universal joint, and a filament acting as a molecular screw. **B.** CryoEM image of *Salmonella* basal body [44]. **C.** A sketch of the bacterial hook basal-body architecture: on the left is the hook basal-body complex of the *Salmonella* H^+-driven motor and on the right is that of the *Vibrio* Na^+-driven motor. The schematic model is drawn based on the electron microscopy (EM) analyses of the *Salmonella* and *Vibrio* motors. *S. enterica* consists of the cytoplasmic (C), membrane/supra-membrane (MS), peptidoglycan (P), lipopolysaccharide (L) rings, as well as a rod. The C, MS, P, and L rings are located in the cytoplasm, the cytoplasmic membrane, peptidoglycan (PG) layer, and the outer membrane, respectively. The rod is practically a driveshaft composed of three proximal rod proteins: FlgB, FlgC, and FlgF, and a distal rod protein (FlgG), and it traverses the periplasmic space [45–47]. The MS–C ring complex is a reversible rotor. FliG, FliM, and FliN form the C ring on the cytoplasmic face of the MS ring, which is formed by a single flagellar protein, FliF [48–50]. FlgI and FlgH assemble around the rod in the PG layer and outer membrane, respectively, forming the LP ring complex that functions as a molecular bushing. The abbreviations in the figure are: IM - inner membrane, OM - outer membrane, and PG - peptidoglycan layer [51].

dissipative allosteric model to describe a non-equilibrium bacterial flagellar motor switch, e.g., involving a dwell-time distribution functions of the CW and CCW states [66]. However, different experiments in clarifying the basic mechanisms have found different CCW and CW interval distributions, with exponential forms [67–69] or the gamma distributions in others [65,70]. The latter observations suggest self-organised steady states, casting doubt on thermal equilibrium-like approaches.

Wang et al. [71] investigated motor switching under various load conditions by addressing different proton motive forces and varying the number of torque-generating stators, which significantly affect the motor torque. They demonstrated that the interval distributions change from exponential to non-exponential shape as the motor torque is varied from zero to a high value. This supports the viewpoint that motor switching is facilitated by a torque-dependent

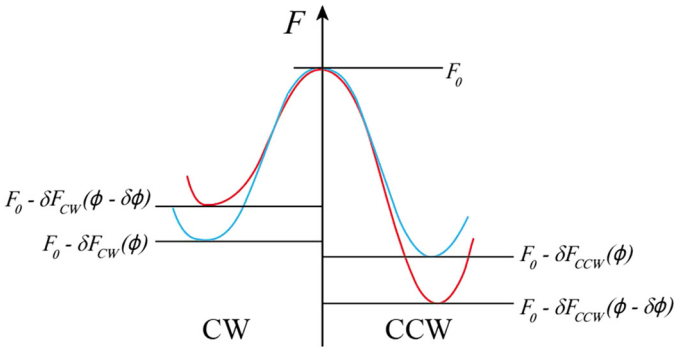

Fig. 6. A thermodynamic model of the flagellar motor isomerisation. The motor fluctuates spontaneously between the CCW and CW states at rates proportional to $e^{-[\delta F_{CW}(\phi)-\delta F_{CCW}(\phi)]/kT}$. As the protonmotive force drops from its normal value ϕ to ϕ-$\delta\phi$, the activation energy $\delta F_{CW}(\phi)$ increases by an amount proportional to δ while the activation energy $\delta F_{CCW}(\phi)$ decreases by a similar amount. Consequently, the probabilities of the transition CCW ⇢ CW and of its reverse, CW ⇢ CCW depend exponentially on δ and are anti-correlated.

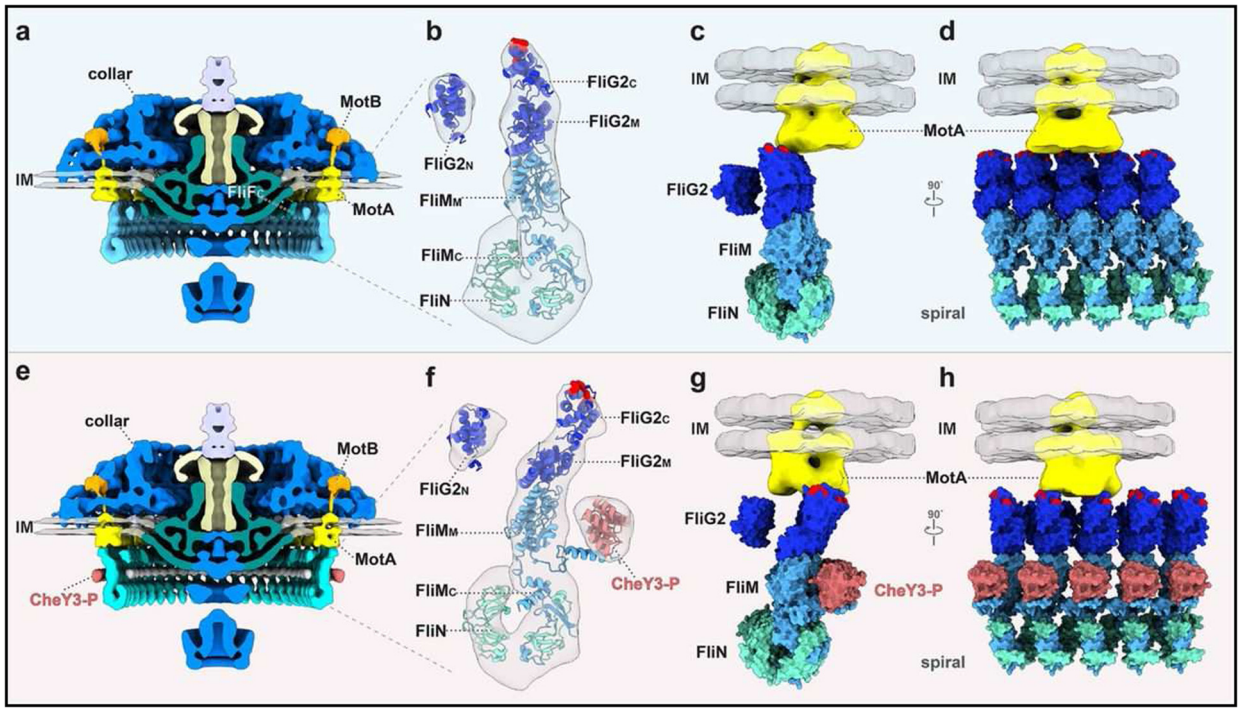

Fig. 7. The molecular architectures of the flagellar motors. The molecular architectures of the flagellar motors with and without the protein CheY3-P. (a) A medial cross-section of the flagellar motor structure without CheY3-P. (b) A model of the C-ring unit shown in (a). FliM and FliN have a stoichiometry of 1:3, and the C-terminal of FliM (FliMC) together with three FliN units form a spiral at the base of the C-ring. (c) Interactions between the bell-shaped stator complex and the C-ring. The charged residues (Lys275, Arg292, Glu299, and Asp300 in red) in FliG2C interact with the inner part of the stator complex. (d) A different view of five C-ring units connected at the based on the C-ring. (e) A medial cross-section of the flagellar motor structure in the presence of CheY3-P. (f) A model of the C-ring unit with CheY3-P binding on the N-terminal of FliM (FliMN). (g) The charged residues (Lys275, Arg292, Glu299, and Asp300 in red) in FliG2C interact with outer part of the stator complex. (h) A different view of five C-ring units occupied by five CheY3-P proteins [58].

non-equilibrium dynamic mechanism. This idea led to the development of the equilibrium conformation spread model by Duke and Bray [64], based on two states with different free energies – one active and one inactive (see Fig. 9). This modified model describes well how the motor's response curve (CW bias versus CheY-P level) shifts to lower CheY-P concentration as the motor torque increases, thereby increasing the motor sensitivity to CheY-P and leading to a mechanism of force sensing, as shown in Fig. 10.

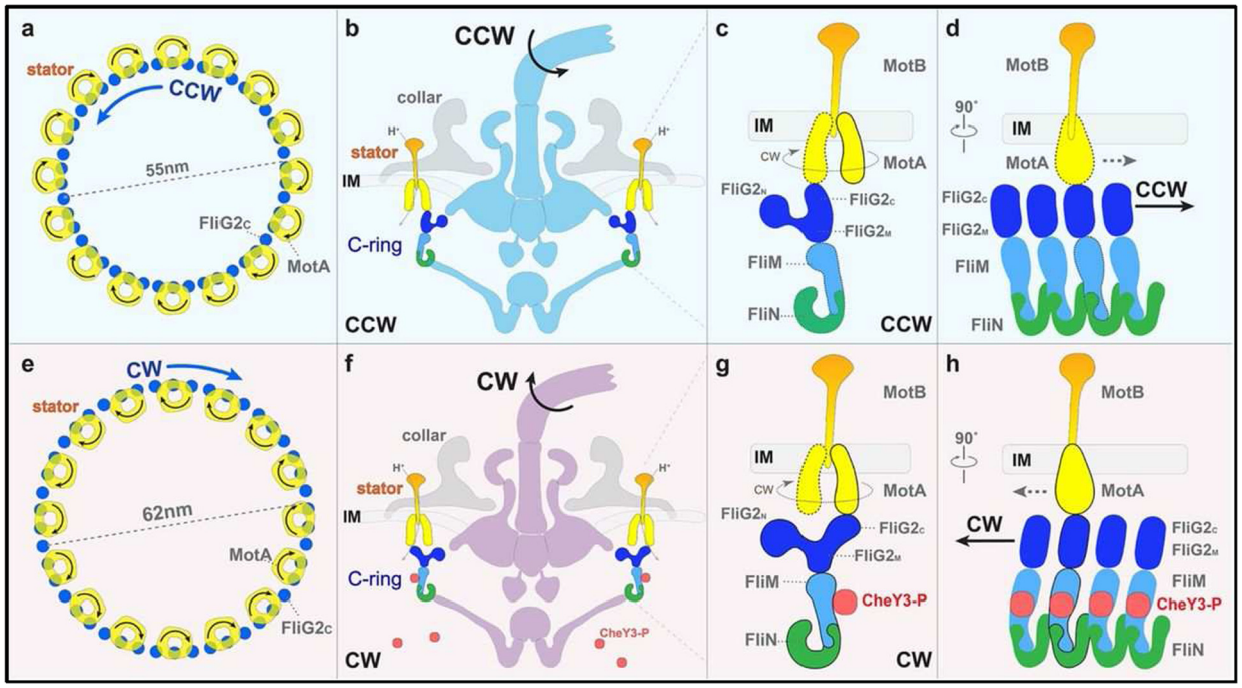

Fig. 8. Model of the rotational switching mechanism. (a, b) Interactions of the stator with FliG2 in the C-ring during CCW rotation. In the default state, in the absence of bound CheY3-P, the FliG2 proteins interact with the inner part of the stator complex (in yellow). The influx of protons through the stator channel causes the cytoplasmic subunits of each stator complex to spin CW. Consequently, the C-ring (blue) is forced to spin CCW. (c) A zoomed-in view of the interaction between the C-ring and the stator complex. (d) A perpendicular view to (c) shows that four C-ring units are connected by FliM/FliN interactions. (e, f) CheY3-P induces conformational changes in the C-ring, leading to altered interactions between the stator and C-ring, thereby causing a switch to CW rotation. The binding of CheY3-P to FliM on the exterior surface of the C-ring, triggers a shift (g) and a tilt (h) of FliG2, giving rise to an interaction of FliG2C with the outer part of the cytoplasmic domain of the stator complex (g). Because the cytoplasmic domain of the stator always spins CW, the C-ring is forced to spin CW (e). During the rotational switch, the spiral ring structure, formed by FliM and FliN, acts as a base that holds the C-ring structure together (d, h) [58].

2.2. *Cooperative stator assembly induces discontinuous transition in bacterial flagellar motor rotation*

The potential threshold for the rotation in *B. Subtilis* is approximately 30 mV. This is lower than the switching threshold of 45 mV between CCW and CW rotation in the flagellar motor, but higher than the potential corresponding to the thermal fluctuations of protons at room temperature $k_BT = 25$ mV, with k_B being Boltzmann's constant. Thus, in addition to CW/CCW switching direction, there is another non-equilibrium transition [52,72,73] between two modes of torque regulation: a quasi-continuous stepwise and a discontinuous jump, both summarised in Fig. 11.

The latter transition is directly related to the structural changes in the stator. As mentioned in the previous section, each stator is a protein complex and contains about ten torque-generating protein units anchored to the cell wall at the perimeter of the rotor. Inspired by a direct observation of steps in ATP-driven molecular motors, Sowa, Rowe [78] managed to measure steps in the flagellar motors and demonstrated the existence of a stepping motion of a Na^+-driven chimeric flagellar motor in *E. coli* at low sodium-motive force and with controlled expression of a small number of stators. They found 26 steps per revolution in the forward direction and 35 in the backward direction. Significantly, these steps occurred in the absence of the flagellar switching protein CheY, suggesting that the differences between the free energies of steps are small.

Ito et al. [79] showed that the steps are hardly affected by changes in the stator-rotor interactions, but that they are sensitive to the stator-stator interaction (Fig. 11a and 11b) and, hence, that it is the latter that drives the stator assembly (Fig. 11c). In other words, in the quasi-continuous step-wise mode the torque in each step is a direct function of the number of bonds between the stators. When there is no bond (the depleted state) there is only one large step from the lowest to the highest torque, resembling a discontinuous torque change. Moreover, the latter transition is accompanied by a hysteresis loop (Fig. 12). This loop ensures a controlled response, securing against over-sensitivity to small

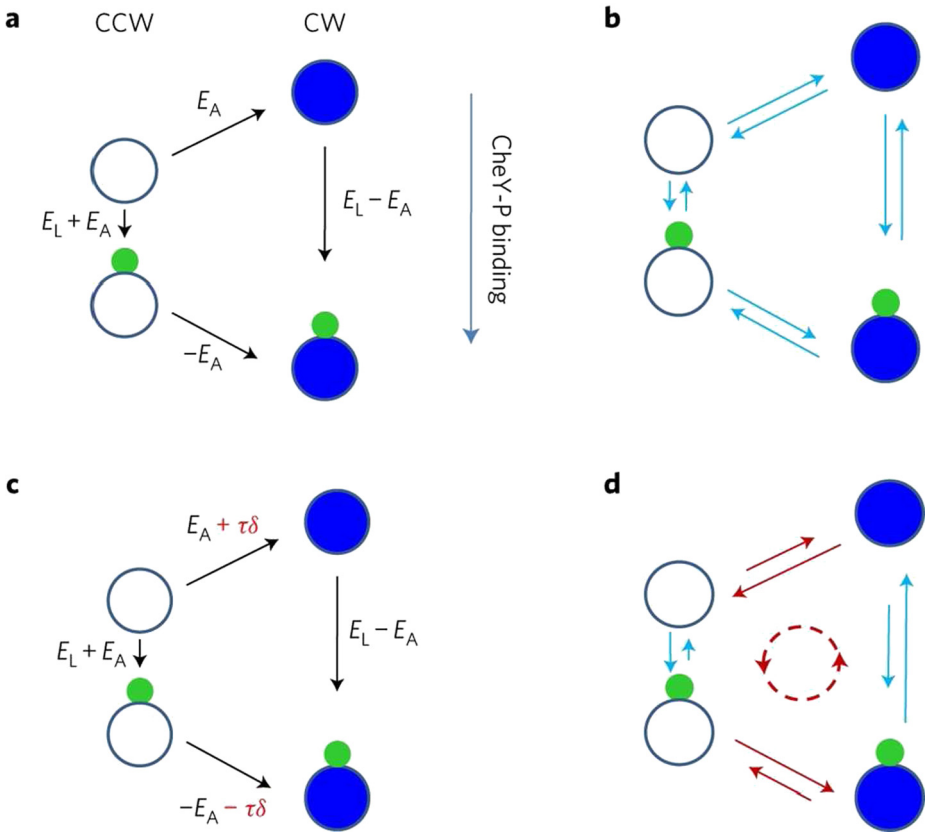

Fig. 9. The free energy diagram of the states of a subunit of the flagellar switch in the equilibrium conformation spread model. **a:** Free energy diagram of the four states of a subunit of the flagellar switch in the equilibrium conformation spread model. Each subunit can be in either CCW or CW states, and has a single binding site for CheY-P. The free energy changes, associated with CheY-P binding, are $E_L + E_A$ and $E_L - E_A$ for the CCW and CW states, respectively. **b:** Detailed balance of the transition rates is satisfied between each pair of states in the equilibrium model. **c:** The addition of the motor torque increases the free energy gap between the CW and CCW states, but takes the process out of equilibrium. **d:** A sketch of the broken detailed balance between CW and CCW states, which results in a cyclic net rate flux (dashed line) [71].

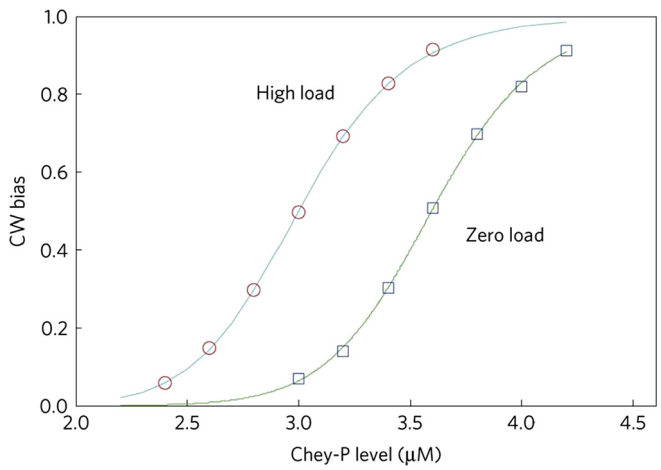

Fig. 10. The motor's response curve, using the non-equilibrium conformation spread model. The motor's response curve (CW bias versus CheY-P level) at zero and high loads, simulated using the non-equilibrium conformation spread model [71].

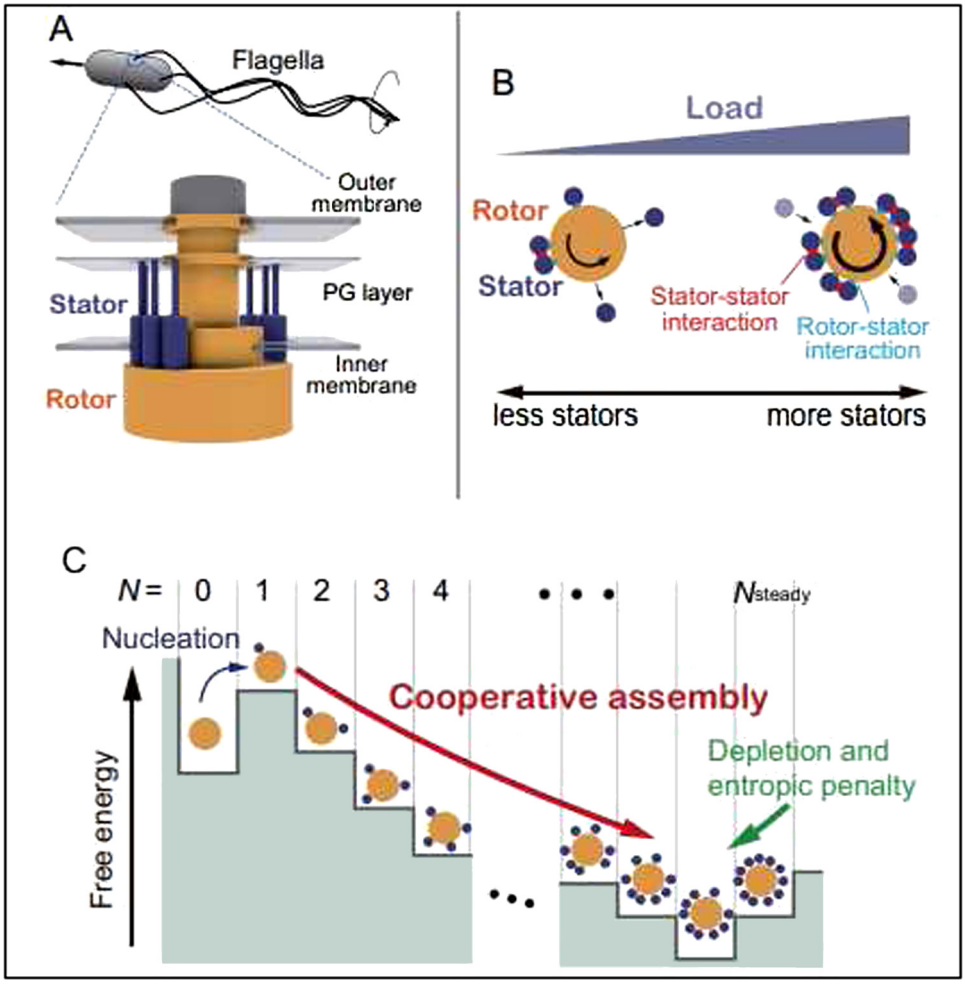

Fig. 11. The Bacterial Flagellar Motor's structure and its kinematics. A. A sketch of the Bacterial Flagellar Motor's complex structure. The motor's size is about 45 nm and it comprises a rotor (light brown) and several stators, which generate torque (purple). The torque is generated at the interface with the rotor and is driven by the free energy released by ion currents through ion channels in the stators. The stators are attached to the peptidoglycan layer at the top of the rotor and exchange energy with its bottom [74–77]. B. The coupling and decoupling of the stators with the motor. These processes are modulated by the load on the rotor and the ion flux through the ion channels. C. A sketch of the inter-stator interaction that drives the dynamics of the stator-assembly.

thermal fluctuations. This mechanism also ensures that the rotor does not rotate during the flagellar-motor assembly. These observations reveal a sophisticated torque regulation.

Further experiments focused on the stator-rotor interaction by studying the stator dynamics under various conditions. Nord, Gachon [80] measured the kinetics of arrival and departure of the stator units in individual motors under varying load and found that the stators assemble at high load and disperse at low load. They also showed that the rate of stator association is independent of the fluid viscosity, while the rate of stator dissociation is viscosity-dependent. Wadhwa, Phillips [81] found that no disassembly of stator units took place at high torque and that all of the stator units were released when the motor was spun at near-zero torque speed. Reverting to high loads led to recruiting stator units and increased the motor speed in the above step-wise manner. Shi, Ma [82] measured the time that motors stay at a constant speed (dwell time) during a particular step at high load at steady state. They observed that the dwell time distribution for any number of stators can be described by two exponentials,

$$P_N(t) = Ae^{-a\tau} + Be^{-b\tau}$$

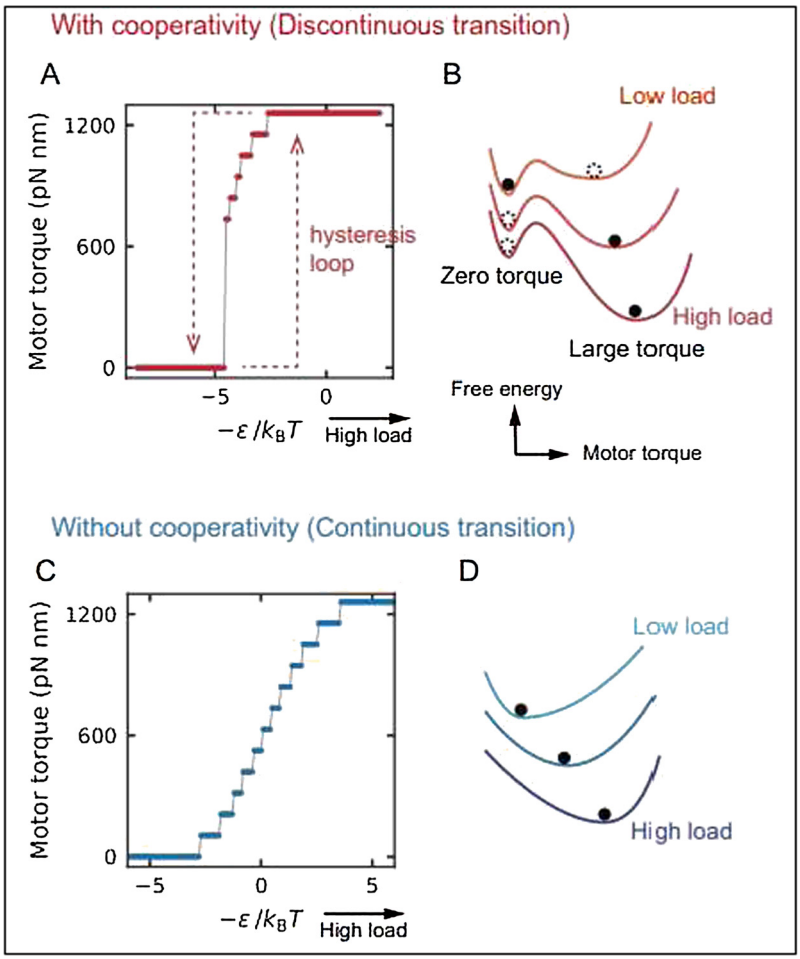

Fig. 12. The motor torque changes in response to the load. The motor torque, which is the sum of the mean torques per stator (∼105 pN nm), changes in response to the load. A. The free energy minimum, calculated numerically with stator-stator interaction. The discontinuous jump in the torque is the fingerprint of a first-order transition. The arrows sketch the direction of the hysteretic process. B. Sketch of the free energy with a metastable state for zero torque and stable state for the large torques. Different graphs correspond to different loads. C. The free energy minimum, calculated numerically without stator-stator interaction. Here the transition is continuous, reminiscent of a second order transition. D. Sketch of the free energy profile in the absence of stator-stator interaction. There is only one stable state.

with $b < a$ the slow-decaying term. While plausibly exponential at long times, the experimental data is quite scattered. Considering only the stator-rotor interactions, they suggested the existence of a hidden state to explain this form. However, they calculate that such a hidden state would lead to a multi-exponential form and, to reconcile with the measurements, they concluded that the decay rate from the hidden state is much larger than the other rates, which overwhelms the distribution and reduces it to two exponentials.

Ito et al. [79] showed that the steps are hardly affected by changes in the stator-rotor interactions, which led Shi et al. [82] to ignore the more dominant effect of the stator-stator interaction. It is the latter that gives rise to the discontinuous transitions, which in turn acts as a binary switch between zero and large torques in response to increasing load.

2.3. Polymorphic transitions in bacterial flagellar filaments

Another component of the bacterial flagellum is the long helical filament, which is a hollow tube 20 nm in diameter and 15-20 μm long. It comprises thousands of copies of the protein flagellin (Fig. 2) [27,29,30,83]. When bacteria swim, the flagella are bundled and in a normal form of a left-handed coil. When the bundle disperses, the bacteria tumble, which leads to a change in the swimming direction. This is accompanied by a structural transition of some of

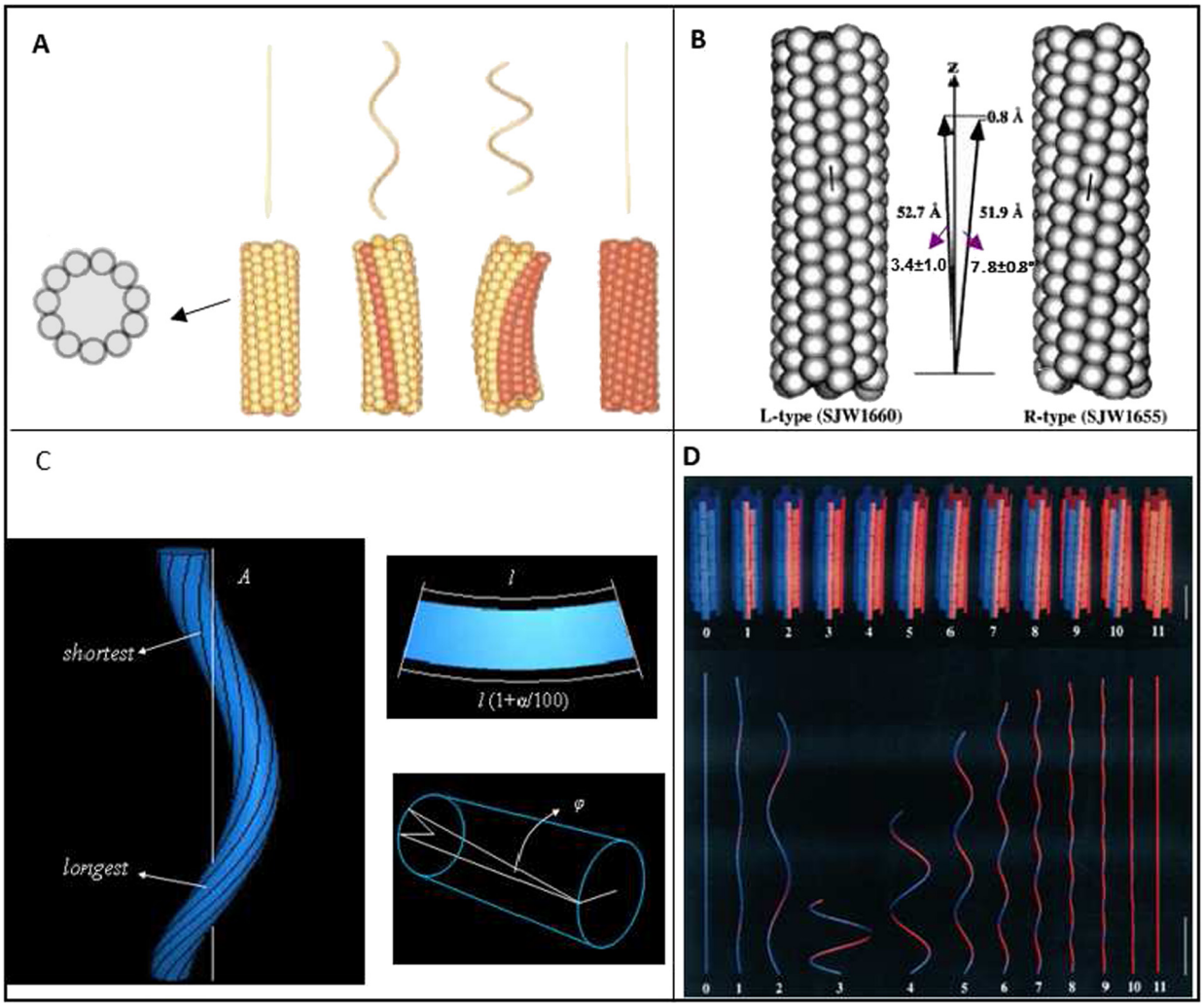

Fig. 13. The molecular structure of the flagellar filament. A. Two state protofilaments model: L-type (yellow) and R-type (red). Different combinations of mixing the two types of protofilaments result in different helical structures of the bacterial flagellar filaments. B. The microstructure of the two kinds of protofilaments with different repeat distance and titled angle. C. Schematics of the bending curvature and the twist of the filament. D. The Polymorphic model of flagellin filaments. Colours around the protofilament interface indicate the type of lattice formed by two adjacent protofilaments, blue are L-type and red are R-type. The numbers below the models indicate the number of the R-type strands. The scale bar is 1 um.

the filaments to a right-handed either semi-coiled or curly forms, as shown in Fig. 3. In total, there are 12 different forms of flagellar filaments with varying diameters and pitch lengths, all of which are sketched in Fig. 13D.

2.3.1. The molecular structure

The flagellar filament contains over 4000 subunits in each helical turn. The large number of protein molecules forming one turn of a helix necessitates a regular and very precise intermolecular arrangement. The first model describing the arrangement of these subunits was developed in 1965, based on electron micrographs of negatively-stained filaments [84]. In that model, a filament consists of eight longitudinal strands, each made of spherical subunits of diameter of about 50 Å. O'Brien and Bennett [85] found that the flagellar filament is actually a tubular bundle of 11 protofilaments, each of which an axial array of subunits. Askura et al. [86–88] proposed in the 1970s a protofilaments model comprising of two helical states of slightly different repeat distances (Fig. 13A). They argued that it is a mixture of these states that gives rise to the 12 different forms of the filament [86–88]. Samatey et al. [29] and Yamashita et al. [89] determined the repeat lengths of the two protofilament: 52.7 Å and 51.9 Å. They also found that the L- type protofilament tilts to the left hand by 3.4±1.0°, while the R-type tilts to the right hand by 7.8±0.8° (see Fig. 14B).

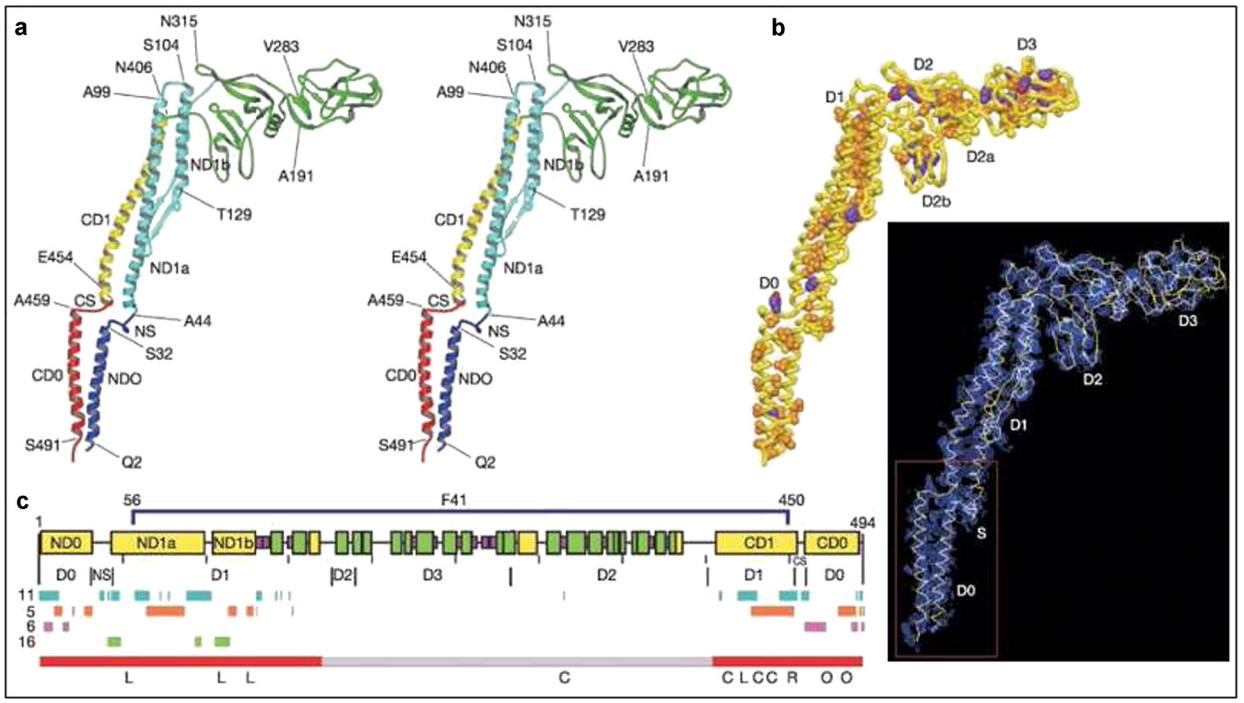

Fig. 14. The flagellin's molecular structure, its Cα backbone, the hydrophobic side-chains, and its structural data. Inset: The flagellin molecule's domains: D0, D1, D2, D3 and the spoke region, labelled S. The full structural details have been detailed in [29].

The differences in the lengths and the tilted angles between the protofilaments lead to the helical formation of the filament. The bending curvature of the filament, α, and the twist angle, φ, are shown in Fig. 13C.

It is interesting to note that the slight difference of only 0.8 Å between the two pitches is responsible for the relative complexity of flagellar filaments through different combinations of the two protofilament states, shown in Fig. 13D. When the motor reverses, the reversal is almost instantaneous, causing the flagella to experience a shear stress that leads to a slight sliding shift between neighbouring protofilaments. This causes several protofilaments to switch into states of shorter repeat length and the helix changes its coiling direction from left to right. The bundle of the flagellar filaments then disperses and the loss of balance leads to tumbling.

2.3.2. Atomic structure

Yonekura, Maki-Yonekura [90] determined the full atomic structure of the R-type filaments from electron cryomicroscopy. Their image data allowed to construct a density map to a resolution of 4 Å, showing an α-helical backbone with several large side chains. The flagellin resembles the letter with a vertical and horizontal dimensions 140 Å and 110 Å, respectively. It consists of four domains connected in series: D0, D1, D2 and D3. These are arranged from the inside of the filament outwards, as shown in Fig. 14. The ribbon diagram of the Cα backbone in Fig. 14a shows the chain folding, and the distribution of hydrophobic side chains. Fig. 14b shows the hydrophobic cores that define the domains D0, D1, D2a, D2b, and D3.

A flagellar filament is organised hierarchically and looks like a hollow cylinder. Flagellin proteins are arranged on top of one another into a protofilament and 11 protofilaments are lined up side by side to form the hollow cylinder. An end-on view of the filament from the flagellum distal end (Fig. 15a) exhibits a concentric double-tubular structure, made of D0 and D1 domains in the densely-packed filament core. Side views from outside and inside the filament (Figs. 15b, 15c), shows D0 and D1 domains interacting closely with internal subunit, both axially and radially. The repeat distance along the axial direction is 51.8 Å, which is the same as the shorter repeat distance of the flagellar protofilament. To study the switching mechanism between L- and R-type repeat, Samatey et al. [29] carried out computer simulations of the local conformational switch in the atomic model of F41. In the simulations, the top subunit of a three-subunit protofilament model was fixed and the bottom subunit was pulled gradually in the axial direction. The aim was to investigate the response of the middle subunit. They found that a discontinuous change in

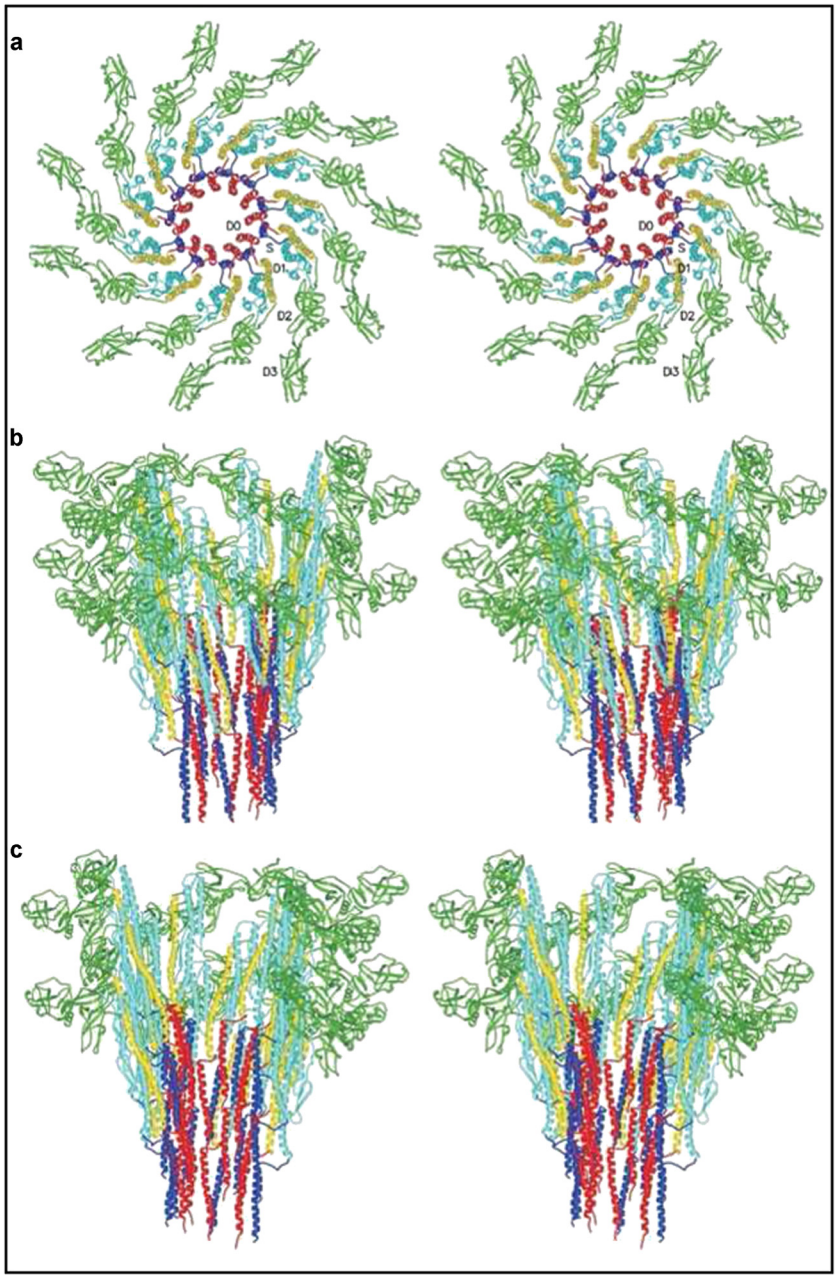

Fig. 15. A ribbon diagram of the Cα backbone of the filament model, with the colour codes as in Fig. 15a. a. End-on view of the filament shows eleven arm-like subunits. b. An outside side view of the filament, from which three protofilaments on the far side have been removed for clarity. c. An inside view of the filament, with three protofilaments removed from the near side. [29].

the conformation of the β-hairpin in domain D1 is responsible for the two-state switching that produces the distinct repeat distances.

Transitions can be induced in two ways: environmental chemical changes and mechanical forces. Placing flagella of wild type bacteria on a chemically designed substrate containing p-fluorophenylalanine, the filaments turn curly [91], as shown in Fig. 16A. A careful procedure can be used to free flagella from the bacterial cells, monomerise them and then reconstitute and purify them to have the same characteristics [92]. Such purified flagella can be depolymerised completely into monomeric flagellin under a number of treatments: heating or exposure to acid, such

as urea and guanidine-HCl. Copolymerisation can then be re-induced [93,94] at certain chemical conditions, such as using 3.0 mg protein/ml and 0.15 M-NaCl in the solutions containing the flagella. Changing the ratios of monomeric and fractionated polymeric flagella in solutions, was shown to give rise to copolymerisation of flagella of distinctly different polymorphic forms. Hotani [94] copolymerised two different flagellins and obtained mixed-type filaments, as shown in Fig. 16B. Kamiya and Asakura [95,96] showed transitions under PH changes in *Salmonella* flagella, which underwent helical reversible transformations both in acidic and alkaline environments (Fig. 16C and 16D). Matsuura et al. [97] studied transformation of straight flagella in mutant *E. Coli* (Fig. 16E) and found that straight and transformed flagella co-existed within some pH ranges. However, no stable forms other than the two were found.

The polymorphic transition can be induced chemically, e.g., either by changing the pH, or by using mutant *E. Coli* bacteria. The mutants have straight flagella owing to either substitutions of some amino acid in the flagellin or by a mutation in the structural gene of the flagellin in the non-motile *E. Coli* strain W3623 ha-177. All these methods control the specific growth of the protofilaments, resulting in various polymorphic flagellar forms [98].

There are also several ways to induce structural changes by mechanical forces. Macnab and Ornston [99] demonstrated that polymorphism emerges when mechanical torsion is applied by the motor. At steady state, such a torque is counter-acted by the medium's viscous torque, with the resulting torque applying torsion to the filament. The polymorphic transition induced in the flagella is to a helical structure that is more tightly wound than the normal one. This is a major structural change that leads to motor reversal, which in turn produces tumbling. Thus, this polymorphic transition plays a key role in the locomotion mechanism. Turner et al. [31] developed a simple procedure for labelling fluorescently cells and filaments, which made possible recording their motion in real time. Using this method to study *E. Coli* cells, they showed that polymorphic transformations occurred in a specific sequence: from normal to semi-coiled to curly1 (Figs. 3b and 3c).

Hotani's experiments on isolated flagella demonstrated the validity of the idea of Macnab [100]. Hotani developed a technique for studying the response of flagellar filaments to mechanical torque *in vitro*. Detached normal flagellar filaments were tethered to a microscope slide and viscous liquid was made to flow past them. This flow produced a transformation of the filament at the fixed end into a right-handed helical form. Two different patterns of behaviour were found: filaments attached to the slide by only a small length at one end appeared to rotate in a clockwise direction, while filaments attached to the slide by longer lengths displayed a more complex behaviour. A cyclic transition between normal and semi-coiled forms is illustrated in Fig. 17a, and cyclic transition between normal and curly forms is illustrated in Fig. 17b.

In these experiments, the transition to the right-handed helix spreads away from the attached end until eventually a reverse transformation back to the normal structure takes place at the attached end. Then the right-handed section moves relatively quickly down the filament and 'escapes' from the free end. In a way, this behaviour resembles the one shown in Fig. 3c, except that the torque is provided by viscous drag of a moving fluid rather than the rotation of the motor. Fig. 18 shows the stages in this repeating three-part pattern of transitions: initiation, growth, and travel**.** By estimating the accumulated tension at the attached end, Hotani obtained an estimate of the accumulated torque. His conclusion was that the torque is responsible for the initiation of both right- and left-handed helices, but that it plays no role in the growth and travel phase. The critical torque for initiating normal to semi-coiled transition was about -11×10^{-19} Nm and the torque for the reverse transition from semi-coiled to normal was 4×10^{-19} Nm. Darnton and Berg [101] showed that the transition of the flagellar filament from normal to hyperextended depends on the rate of loading They pulled at filaments using oscillatory pulling-releasing force cycles. Rapid pulling during one cycle at 0.4 μm/s causes the filament to behave as a simple elastic, hysteresis-free, spring in 9 of 19 cycles without any polymorphic transition. In the other 10 cycles, a polymorphic transition was observed. Reducing the pulling rate to 0.04 μm/s gave rise to a transition on each cycle.

2.3.3. Mechanical construction

Calladine et al. [86,88,98,103] modelled the polymorphic mechanism of the filament by assuming two states for the subunit conformation. The two states correspond to the sub-units connecting at either point α or point β in the top left inset of Fig. 19. Connecting at point α generates an L-type protofilament and connecting at point β generates an R-type (see Fig. 14). Different sequences of these connections lead to different configurations of the flagella. Fig. 19 depicts 11 nearly vertical lines having 12 distinct packing states of vertical 'strands' of connections, labelled f_0, f_1, $\ldots$, f_{11}.

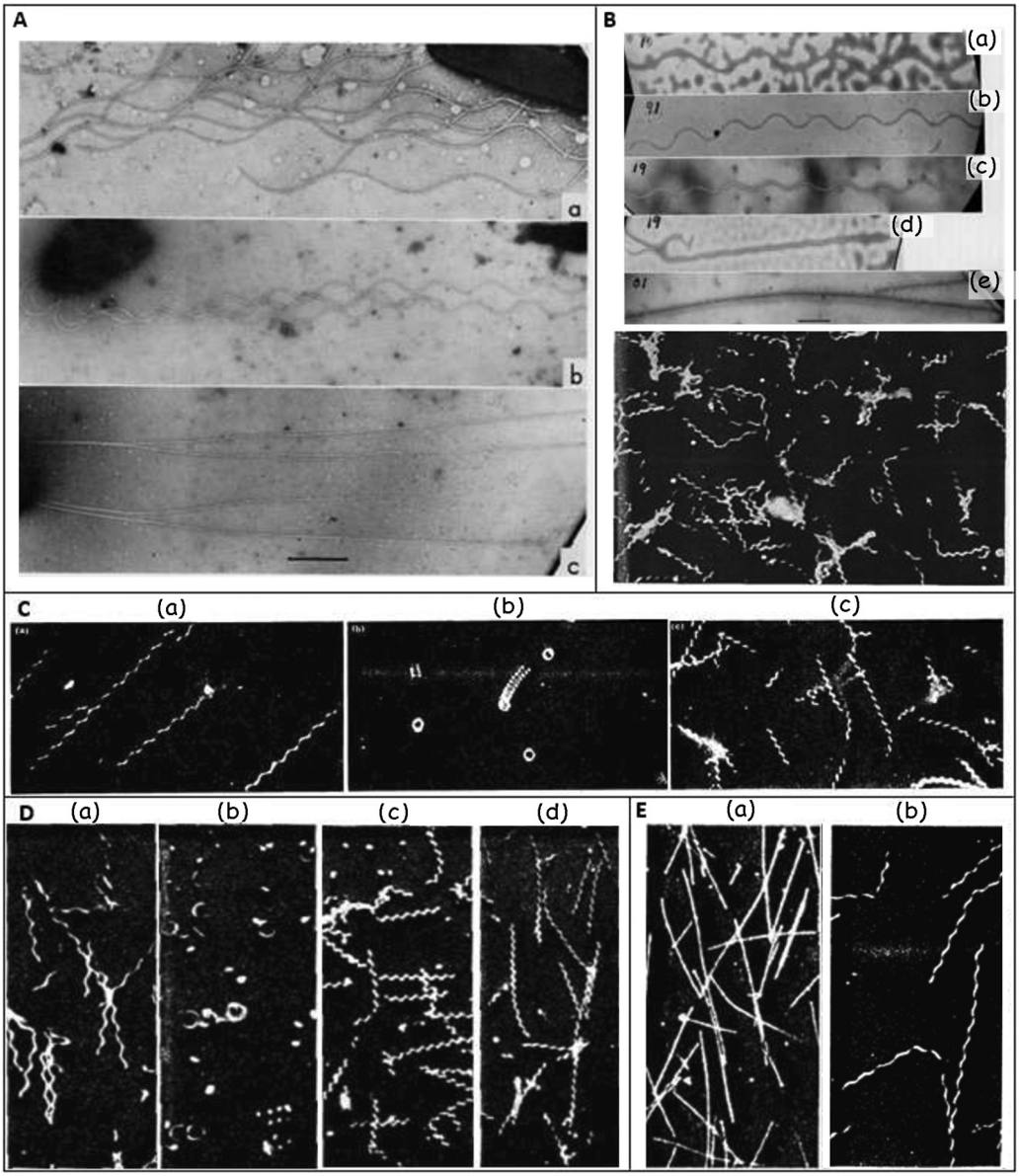

Fig. 16. Polymorphic transitions in bacterial flagellar filament in response to chemical changes. **A. (a)**. Normal-type *Salmonella* flagellar filaments, produced by the wild type SJ25 strain. **(b).** Curling of the same flagellar filaments, produced by the curly mutant SJ30 strain. **(c).** The straight mutant SJ814 produces straight flagellar filaments. The shown scale is 1 μm and it applies to all three images. B. Different stable waveform conformations of the flagellin copolymers. Shown are: two kinds of normally flagellated strains SJ670 (i) and SJ25 (n), a curly flagellar mutant SJ30 (c), and a straight flagellar mutant SJ814 (s). The waveforms were characterised by the contour length contained in one period, L, and the amplitude, h. Homogeneous filaments of i- and n-flagellins usually exhibit a long period waveform while the s-flagellin is straight. Mixing the i- and n-flagellins with s, the values of both L and h in the copolymers $(i + s)$ and $(n + s)$ decrease with increasing concentration of s-monomers. The change, however, is not gradual but takes place via a number of morphological transitions. **B.** Top panel: Five stable conformations of the copolymers $(i + s)$. **(a).** Type I filament in a mixture i:s=1:0; **(b).** type II filament in a mixture i:s=9: 1; **(c).** type III filaments in a mixture i:s=1:3; **(d).** type IV filament contained in 1:9; **(e).** a straight filament in a mixture i:s=0:1. The scale, 1 μm, is shown in B(e). B. Bottom panel: the mixture of the type II and type I filaments, at magnification 500x. **C.** Dark-field light micrographs of i-flagella in acidic environment at magnification 600x. **(a).** Normal form observed at pH 7.0; **(b).** coiled form at pH 4.7; **(c).** curly form at pH 4.1. The flagella were suspended in a solution of 0.1 M NaCl, 1 mM acetic acid, and 1 mM sodium acetate. The suspension's pH was varied by adding either 1 M HCI or 1 M NaOH, **D.** Dark-field light micrographs of i-flagella in an alkaline environment at magnification 600x. (a) Normal form at pH 7.0, (b) coiled at pH 11.0, (c) Curly I at pH 12.0, (d) curly II at pH 12.5. **E.** The non-motile strain W3623 ha-177 of *E. Coli* produces straight flagella as a result of a mutation in the structural gene for the flagellin. Shown are dark-field light micrographs of flagella from mutant *E. Coli* suspended in 0.1 M NaCl solutions at magnification 500x at: (a) pH6.0, (b) pH 8.0. [91–97].

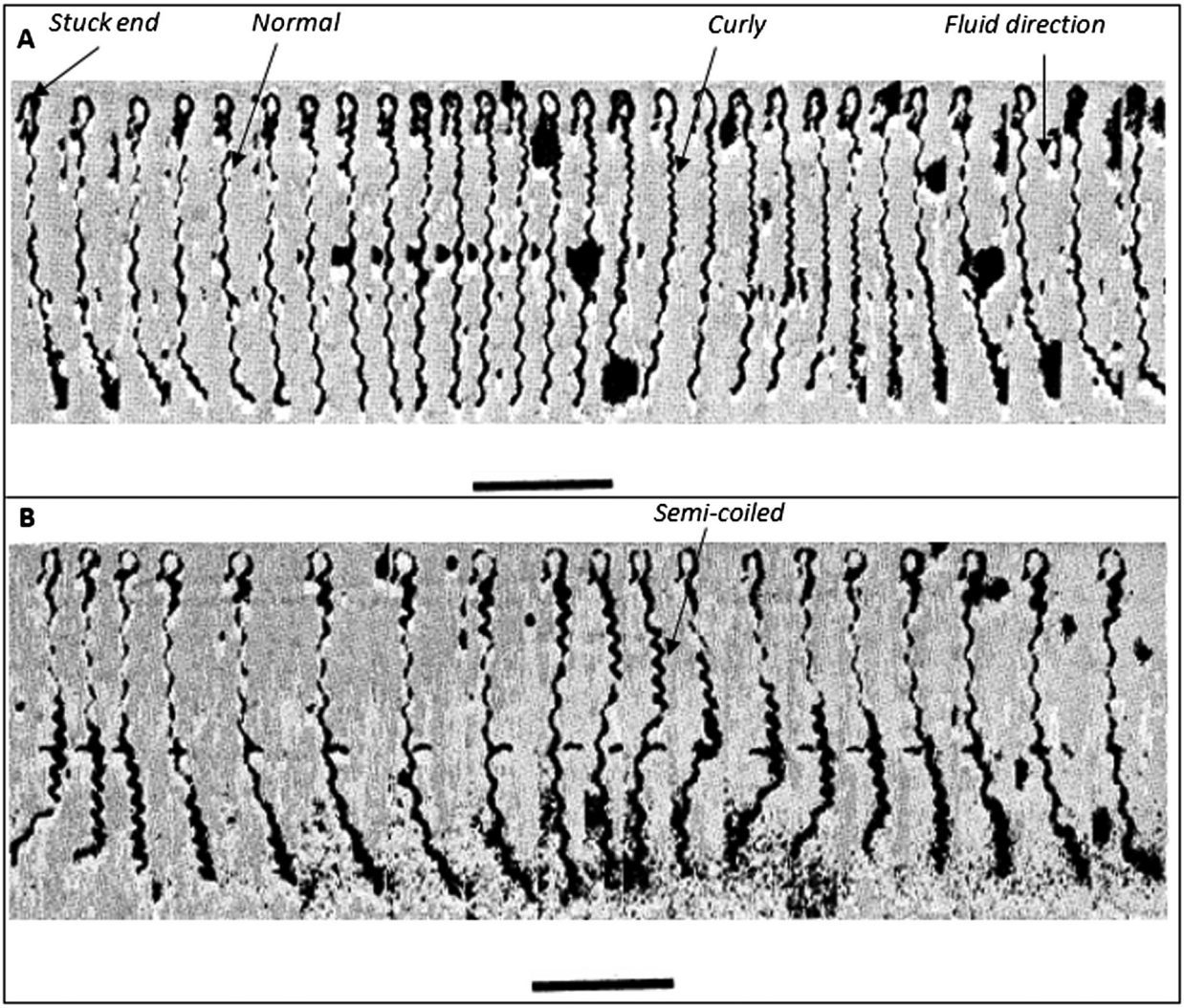

Fig. 17. A. The cyclic response of a flagellar filament, attached to a glass surface at its top portion. Successive snapshots (from left to right at intervals of 5/9 s) of the filament's cyclic conformation changes between normal and semi-coiled, as a viscous fluid flows from top to bottom. B. The cyclic transformation between normal and curly forms in the same set-up as in A, with successive frames from left to right, taking in total 36 s. [100].

Hasegawa et al. [104] extended the above model by explaining the roles that the R-type and the L-type protofilaments play in determining the positions of the connecting points, as illustrated in Fig. 20. Their model differs from that of Calladine et al., in which the subunit has elastic deformation with identical bonding energy at different connection points. They name this quasi-equivalence. In contrast, the subunit in Hasegawa et al. involves elastic deformations with different bonding energies at different connecting points, which they named non-equivalence. In this model, the mechanical energy is minimised when short protofilaments are next to short protofilaments and long protofilaments are next to long protofilaments [86].

2.3.4. Continuum theoretical models

A number of continuum models for different chiral states exist. Goldstein et al. [105] and Coombs et al. [106] proposed a bi-stable energy function to describe the transitions between the two helical states phases observed in Hotani's experiment. Srigiriraju and Powers [107] and Srikanth et al. [108] proposed a continuum model for the polymorphism of the filament, based on molecular switches and an elastic mismatch strain between the inner and outer cores of the flagellum. Speier et al. [109] and Vogel and Stark [110] proposed a coarse-grained model based on

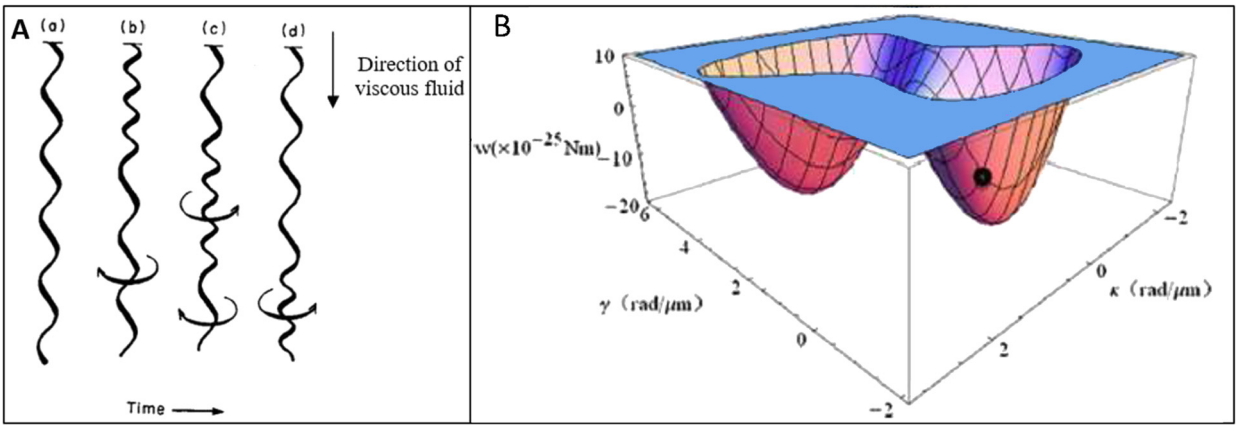

Fig. 18. The cyclic phase transition in the filament between normal and semi-coiled form, and the double well free energy of the filament. A. The rotation direction of different sections, illustrated by arrows, of the filament, as it undergoes the cyclic transformation. The longer pitch in (a) represents a normal helical form while the shorter represents either the curly or semi-coiled right-handed helices. The latter are initiated in (b) and travel from the attached top end down (c)-(d) [100]. B. A double-well free energy as a function of twist and curvature. The two wells represent two stable phases: normal and semi-coiled [102].

an elastic network of rigid bodies and used Ising Hamiltonian to represent the two states of the flagellin protein. Wada and Netz [111] introduced a bi-stable helical filament model that accounts for different elastic monomeric states by a discrete Ising-like spin variable along the arclength. Using a hybrid of Brownian dynamics Monte–Carlo simulations, they showed that filament phase transition depends on the pulling rate. Wang et al. [102,112–116] used the time dependent Ginzburg–Landau continuum model to analyse Hotani's experiment [100]. They modelled the free energy, F, as a function of the twist, τ, and the curvature, k, both per unit length,

$$F = -a\tau^2 + b\tau^4 + dk^4.$$

This free energy has two minima for the normal and semi-coiled states, shown in Fig. 19b for $a = d = 8.2 \times 10^{-25}$ and $b = 1 \times 10^{-25}$. The strain gradient energy density in the τ-k plane is

$$G = g_1 \left(\frac{\partial k}{\partial s}\right)^2 + g_2 \left(\frac{\partial \tau}{\partial s}\right)^2 + g_3 \frac{\partial k}{\partial s}\frac{\partial \tau}{\partial s},$$

in which g_1, g_2, and g_3 are material-dependent coefficients that are functions of the interface thickness. Assuming an inextensible 20 μm-long filament and $g_1 = g_2 = g_3 \equiv g$, they used these equations within a Finite Element Method to simulate by the transition of the filament from an initial normal state, N, to a semi-coiled state, SC. Their results are presented in Fig. 21. Specifically, they simulated different aspects of the filament's transition and showed the effects of the rotation angle loading rate, the bending deflection loading rate, and the magnitude of the energy barrier, on the transition. The equilibrium twists of the N and SC states are approximately 0 rad/μm and 4 rad/μm, and their equilibrium curvatures are approximately 0 rad/μm and 1.2 rad/μm, respectively. The torque-twist and bending-curvature curves of a filament at the loading end are shown in Figs. 21a and 21b. After an initial elastic deformation of the N phase, the torque drops to a constant value that does not change with increasing twist, Fig. 21a. Similarly, the bending moment drops to a constant value that does not change with increasing curvature, Fig. 21b. These constant values correspond to a nucleation of the SC phase and its growth along the filament. During this growth the N and SC phases coexist, which can be observed in Figs. 21e and 21f. This plateau is the fingerprint of a first-order phase transition, e.g., the temperature plateau during water boiling at atmospheric pressure. As soon as the SC phase boundary reaches the end of the filament, the torque and bending decrease momentarily, which corresponds to the disappearance of the interface between the phases. Further loading then leads to elastic deformation of the remaining SC phase.

The nucleation and growth of the SC state along the filament upon increase of the rotation angle and the bending deflection, can be clearly observed in Figs. 21e and 21f, respectively. When the two states coexist, they are separated by a transition zone of about 1 μm. Loading-unloading cycles of the rotation angle and bending deflection are shown in Figs. 21c and 21d. Both torque and bending drop down in the loading curve (corresponding to phase nucleation,

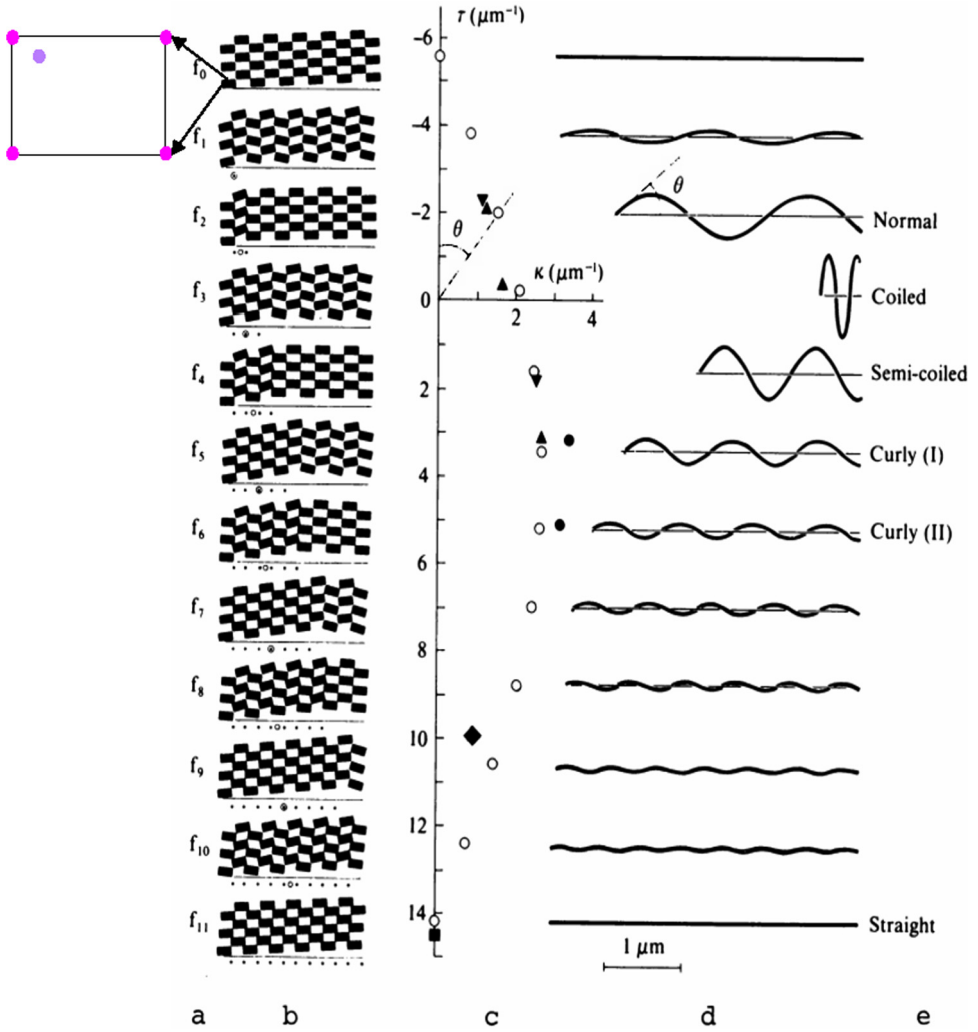

Fig. 19. The relations between the sub-unit structure and the filament helical phases. (a) and (b): Alternative arrangements of the outer part of the subunit. The upper left corner of each subunit has two distinct bonding sites, to which the adjacent subunit can connect. All twelve possible surface packing patterns are shown, designated f_i, with $i = 0 - 11$ the number of longitudinal strands. The patterns are generated by subunit connecting to two distinct bonding sites, shown in the top left inset. The strands marked ● are slightly shorter than the others, causing the filament to curve such that their conformation minimises strain energy. Tilting of longitudinal columns, such as the left-hand tilt in f10, twists the filament. (c): The curvature, κ, against the twist, τ, corresponding to the structures in (b). The curvature and twist of the ideal waveforms are denoted by open circles, o, and also correspond to the patterns in (b). Included are: data from dark-field light microscopy [95] of the waveforms of filaments constructed from i-flagellin (▲), $n-$ flagellin (▼), and c-flagellin (●); data from [85] on the twist of straight filaments built by s-flagellin (■); and data on waveform IV (◆) from [91,93] (shown in Fig. 17). (d) The shapes of the 12 ideal waveforms, corresponding to (b) and (c), drawn for a contour length of 4 mm. (e) Conventional names of the waveforms. The absence of name indicates theoretically predicted waveforms that have not been observed yet [88].

with the arrow down) and jump up in the unloading curve (corresponding to phase disappearance, with the arrow up). The formation of a hysteresis-like loop by the loading and unloading curves suggests that energy is dissipated during the nucleation and disappearance stages of the process, most likely in the form of elastic vibrations and heat.

The twist and curvature profiles, as the rotation angle and the bending deflection are applied, are shown in Figs. 21g and 21h, respectively. As the loading is reversed (unloading) the SC phase shrinks. When this phase shrinks to roughly twice the transition zone thickness, the SC phase suddenly disappears, which takes place during the unloading steps 10 μm → 5 μm → 0 μm, and the filament reverts to the N state. The value of g has to be adjusted to $g = 0.08$ μm to obtain a quantitative agreement with the thickness of the transition zone and the twist profile in Fig. 21i. But fitting

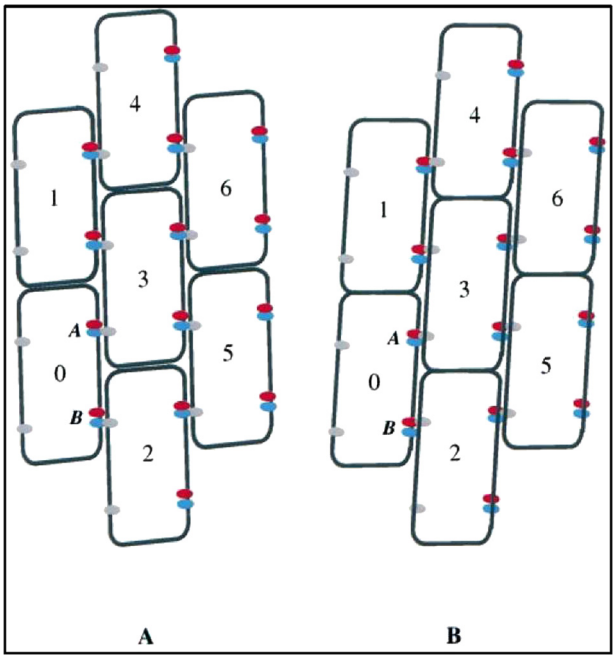

Fig. 20. A polymorphism switching model. A possible model of the switching involved in flagellar polymorphism due to the interactions of the subunits in the outer tube. The subunits in A and B are, respectively, L- and R-types and the filament axis is vertical, with each elongated numbered block representing a α-helical bundles, aligned roughly parallel to the filament axis. This model hypothesises two different binding regions between the subunits – A and B. Gray-blue and grey-red interactions represent, respectively, L- and R-types packings. The different distances between the red and blue sites in the A and B regions, 1.8 Å and 2.6 Å, respectively, lead to a longer distance between subunits in the latter along the protofilament, i.e., the subunits 0 and 1 [104]. The strain energy is minimised when short protofilaments are next to one another and long protofilaments are next to one another [86].

to Fig. 21e requires $g = 1$ μm. This may suggest that setting $g_1 = g_2 = g_3$ is possibly an over-simplification and a model with non-equal such coefficients may be more suitable. Reducing g effectively reduces the interface energy of the transition zone between the two states and makes it narrower. In turn, this reduction affects the nucleation and disappearance rates of the SC state. Thus, the nature of the transition between the N and SC states is fully determined by these coefficients.

The development of the twist profile with time was simulated at small time steps of $\delta t = 0.5$ s and it is shown in Fig. 21k. Both states coexist initially, each in its own equilibrium profile configuration (black line t = 0 in Fig. 22k). The twists of the two coexisting phases are at the equilibrium values: 0 rad/μm and 4 rad/μm, respectively. The total torsion angle of the filament is 24 rad. It can be observed in Fig. 21k that, when a step torsion loading is applied at $\delta t = 0.02$ s (red line), the twist increases instantaneously at both phases.

Fig. 21l shows that a rapid increase in the twist angle loading quenches the configuration and suppresses the transition. Initially, the two phases coexist in their equilibrium twist values, 0 rad/μm and 4 rad/μm, respectively. A rapid increase of the total twist angle to 24 rad at t=0, gives rise to no significant change in the twist profile along the filament. The SC phase does not grow because the loading time is much smaller than the response time required for the transition to proceed. This is analogous to quenching in conventional phase transitions, e.g., in metals.

2.4. Phenotypic switching in bacteria

Prokhnevsky et al. [117] defined bacterial development as a "series of stable and meta-stable changes in the form and function of a cell, where those changes are part of normal life cycle of the cell". Bacterial growth has been traditionally viewed as the result of symmetrical cell division into genetically identical siblings. However, it has been known for a while now that phenotypic variation is a widespread phenomenon in the isogenic populations. The phenotypic variation has been attracting much attention because of its relevance for cellular differentiation and its implications for the treatment of bacterial infections [118]. Phenotypic switching is one of the mechanisms by which

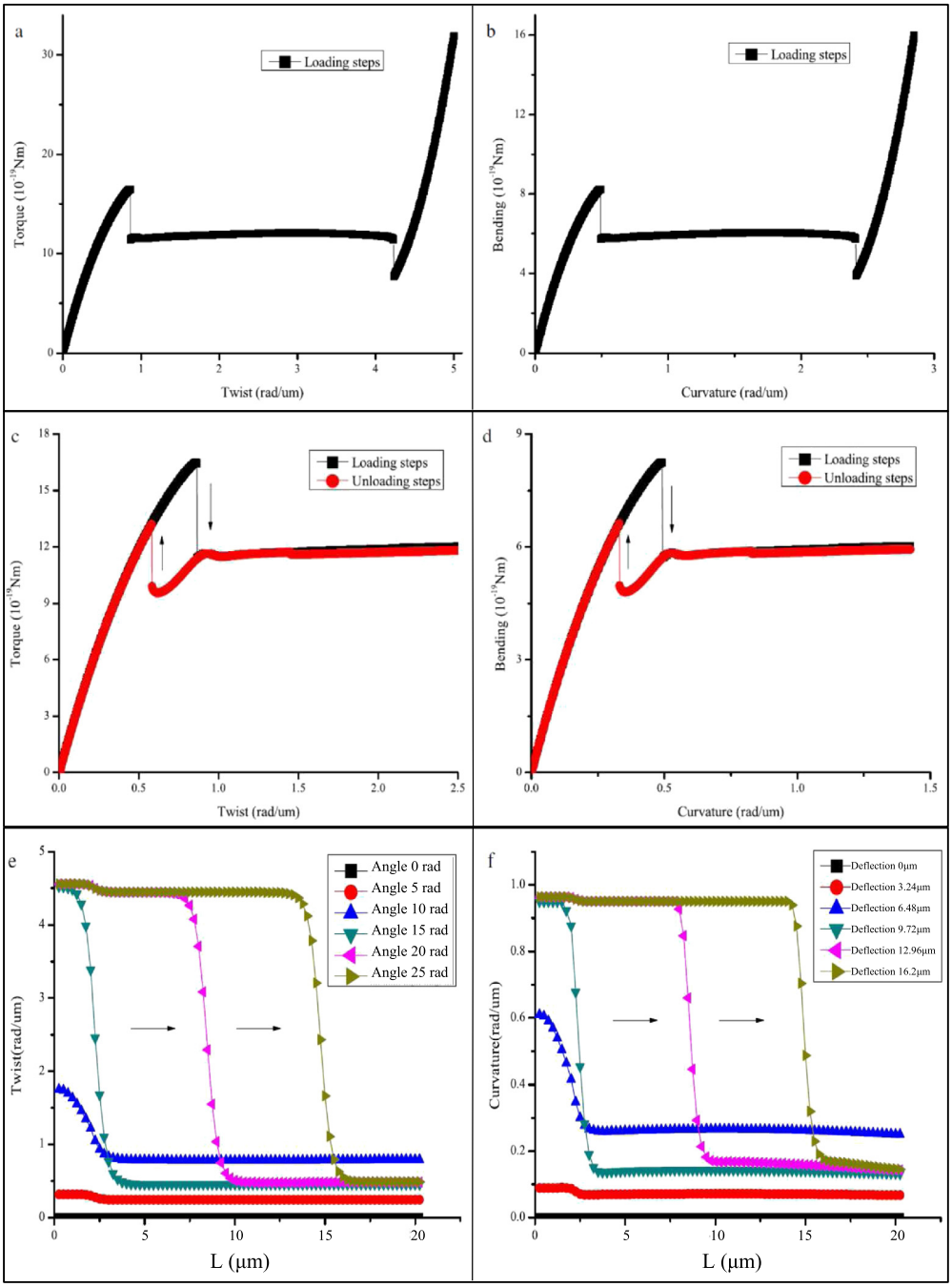

Fig. 21. The mechanical loading-deformation characteristics of a filament. The deformation characteristics of a filament, of length 20 mm, under different types of loading. (a) Torque-twist curve of a filament under proportional loading, i.e., a load increase of the rotation angle and bending deflection by the same ratio. (b) Bending-curvature curve of a filament under proportional loading. (c) The hysteretic torque-twist curve of proportional loading and unloading of rotation angle and bending deflection. (d) The hysteretic bending-curvature curve of proportional loading and unloading. (e) The twist profile, as a function of position along the filament, L, for g = 1 mm (see text) under proportional loading. (f) Curvature profile for g = 1 mm under the same proportional loading; (g) Twist profile of a filament under the same proportional unloading; (h) Curvature profile of a filament under the same proportional unloading. (i) Simulated twist profile for g = 0.08 mm at different torsion loadings – in contrast to (e), a sharp interface is obtained. (j) Torque–twist response of bacterial filament under slow and fast twist loading. (k) Evolution of the twist distribution of an initial two-phase coexistent state after a slow torsion loading, carried out over a duration that is much longer than the material characteristic time t_r. Here, $\delta t = 0.5$ s. (l) Torsion loading, applied to an initial two-phase coexistent state on a time scale much shorter than the material characteristic time. The evolution of the twist distribution is no different than in an elastic filament. Here, $\delta t = 0.02$ s.

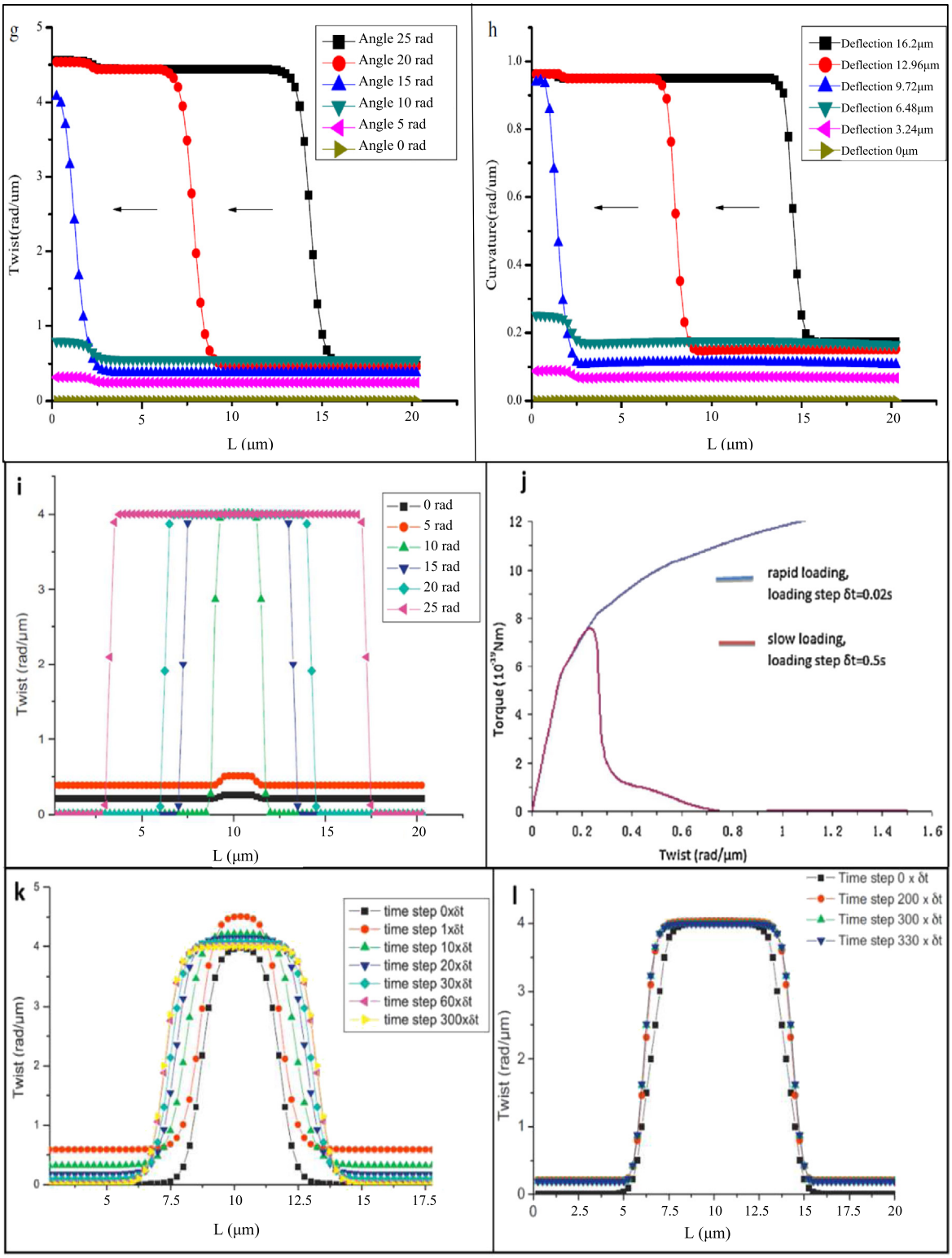

Fig. 21. (*continued*)

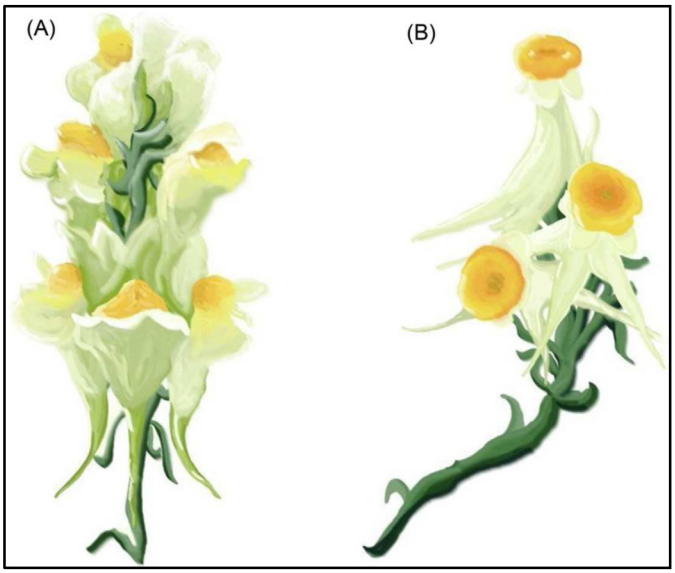

Fig. 22. Pelorism *in Linaria vulgaris*. (A) Common form of flower shape in Linaria. The petals form a corolla tube with a distinct dorsoventral asymmetry. (B) Peloric flower shape: the petals form five spurs with a distinct radial symmetry [120].

bacteria survive in ever changing environmental conditions and it can be induced by either inheritance or epigenetics. This mechanism is not limited to bacteria. One of the oldest examples of phenotypic switching was discovered by Zioberg in *Linaria vulgaris* (Fig. 22) [119]. The morphology of the flower shape of this phenotype is completely different from the more common form of five petals united to form a corolla tube (Fig. 22A). In contrast, the petal of the phenotype found by Zioberg form five spurs with a distinct radial symmetry (Fig. 22B).

Heritable variation of phenotypic switching is often caused by random mutations in the DNA sequence, which have a beneficial impact on reproductive success. Depending on their fitness effect and the population size and structure, the frequency of genotypes changes over time determines the evolution process [120]. The first attempts to catalogue and document phenotypic variation began at 17th century with John Ray, who classified groups depending on their similarities, and termed as species any group that shares characteristics, which distinguish them from another group [121]. By realising that such characteristics must be stably transmitted from parents to their offspring, he was one of the first to recognise the connection between inheritance and inter-species variation [122]. For Darwin, variation between individuals is the basis of the evolutionary process: “Owing to this struggle of life, any variation, however slight and from whatever cause proceeding, if it be in any degree profitable to an individual of any species..., if useful, is preserved” [123]. At about the same time, Mendel found phenotypic variations in plants, pointing out that the particular inheritance is determined by independent particles [124]. Johannsen coined in the 19th century the terms ‘genes’, ‘phenotypes’, for observable characteristics of individuals, and ‘genotype’ for underlying genetic determinants [13]. De Vries defined mutations as any changes in observable characters that deviate from those found in other individuals of the same species [125].

Yet, a phenotype needs not originate only in a nucleotide sequence, as an outcome of a myriad of complex interactions between the organism and the environment. Since the beginning of the 20th century, it has been accepted that the same genotype can produce different phenotypes, depending on the environment that the organism is experiencing during the development, a phenomenon known as phenotypic plasticity [126]. Moreover, phenotypic switching can also occur, namely, the phenotype of an organism switching between generations at a certain rate. This can happen either because of the stochastic nature of the underlying developmental mechanisms or it can be induced by environmental cues, such as temporal fluctuations in pressure [127], molecular noise in metabolic enzyme expression, positive feedback loops, and asymmetric partitioning of cellular components during cell division [128]. The concept of epigenetic landscape was introduced by C. Waddington to explain phenotypic plasticity and its possible contribution to evolution [129]. In modern terms, epigenetic inheritance comprises many different mechanisms that modulate gene expression and cause production of different phenotypes. Intriguingly, some of which can be inherited seemingly in-

dependently of the underlying DNA sequence. In particular, phenotypic switching is one of the mechanisms by which bacteria adapt relatively rapidly to ever-changing environmental conditions, speeding up microbial evolution [130].

2.5. Lifestyle switch from free-living bacteria to biofilms

Bacteria constantly face a multitude of chemical and physical stresses associated with external environments and host-specific niches. To survive, they have evolved molecular mechanisms for altering their lifestyles in response to changes in environmental conditions. For example, free-living bacteria can switch their lifestyle to undergo development to form matrix-encased aggregates called biofilms on different abiotic and biotic surfaces [131]. We define the ability to shift from a planktonic lifestyle to a multicellular community as a 'lifestyle switch', which is observed in a majority of chronic bacterial infections [132]. The regulation of lifestyle switches in bacterial pathogens is important to enable successful pathogenesis.

Bacteria often exist in organised communities - biofilms – consisting of cells and EP [133], illustrated in Fig. 4. Biofilm formation is an efficient microbial strategy to persist in harsh environments. The advantages of bacteria within a biofilm relative to their planktonic counterparts are several: increased antimicrobial resistance, protection against predation, dehydration, and phagocytose [134]. Biofilms are the result of free-living bacteria attaching irreversibly to either an abiotic or a biotic surface, as well as of bacterial growth and division to form a mature biofilm. During the growth of a biofilm, bacteria adopt a biofilm-specific phenotype that is radically different from that expressed in the corresponding planktonic cells [135]. Biofilms are a heterogeneous aggregation of microbial phenotypes [136, 137] that live together as a community, coordinating group activities, such as circulation, dispersion, and aggregate movement [138–142]. The different phenotypes rely on one another and interact cooperatively toward the success of the entire community [143].

2.6. Phenotype switching in biofilms

Phenotype switching in biofilms has been observed in a wide range of bacterial species, including both Gram-negative and Gram-positive bacteria [144], which differ significantly in the structure and thickness of their cell walls [145]. Several studies have demonstrated that genetic variants arise in biofilms through mutation or recombination. These variants have been detected primarily as changes in the colony morphology of subpopulations of cells following biofilm growth. Following the growth of the parent strain in biofilms, small fractions of isolated strains exhibit colony morphologies that differ distinctly from the parent. Examples include the small rough or wrinkly variants of *Pseudomonas aeruginosa* [136,146], the small non-mucoid variants of *Streptococcus pneumonia* [147] and the rugose colony type of *Vibrio cholera* [148]. Because variants can constitute 10% or more of a biofilm population within a few days of being formed from a homogenous inoculum [136,149], it is unlikely that mutation processes alone are responsible for the accumulation of variants. Mutation and genetic rearrangements probably generate variants that are then enhanced through natural selection in the local biofilm environment. In a mixed-species biofilm, genetic changes during biofilm development can lead to the evolution of species interactions [150].

Stochastic gene expression may also lead to phenotype variation. In contrast to changes in DNA sequences, some subpopulations of cells may express genes in a stochastic manner, rather than in response to a particular environmental cue, and therefore differently from the larger population. Baty et al. [151,152] studied the expression of a chitinase gene (chiA), in a marine *Pseudoalteromonas* species, in young biofilms that were attached to chitin and silicone films. They observed that individual cells that expressed strongly chiA could be found adjacent to cells that did not express chiA. They and suggested that this differential expression reflects a strategy of 'division of labour' by bacterial subpopulations. The very thinness of those biofilms meant that cells exhibiting differential activity were very close to one another, which makes it very likely that they experienced almost identical chemical environments. This then suggests, again, that gene expression in an originally clonal population is driven by a bistable mechanism. Bistability might indeed explain the occurrence of subsets of bacterial cells, called persister cells, in biofilms [153–155]. Persister cells are proposed to be a subpopulation of cells that have an enhanced resistance to antibiotics. Using a microfluidics approach, this idea was substantiated for a clonal population of *E. Coli* at the single-cell level [156]. This was demonstrated by first noting that cells experiencing nearly identical environmental conditions divided at different rates [156,157] and then that the much slower-dividing or non-dividing cells survived antibiotic treatment. When the antibiotic treatment was removed those cells switched to rapid growth. There is currently active research to identify the genetic basis of persistence [158–161].

B. Subtilis practises a different strategy forming, biofilms through a series of phenotype switches, with three main phenotypes comprising 90% of all cell types. This species is one of the most intensively studied Gram-positive bacteria, being a good model organism to study biofilm formation [162]. *B. Subtilis* is useful for treatments for gastric and urinary tract diseases [163], for improving agricultural yields, as well as an ingredient in the production of a Japanese delicacy known as 'natto' [164]. Its three main phenotypes during biofilm growth are: motile cells, cells that produce extracellular matrix, and cells that differentiate into spores. The motile cells have flagella that enable them to swim in solution or to swarm along wet surfaces [165,166]. Matrix-producing cells produce a mixture of amyloid proteins and exopolysaccharides that hold the community together [34]. Spores are metabolically inactive, resistant to heat and antibiotics, and can germinate under certain favourable conditions [167,168]. These three phenotypes are different in their gene expressions and together they account for nearly all of the cells [169]. Additional cell states include competent cells, which are able to take up extracellular DNA from their environment [170,171], and cannibalistic cells, which can kill their sister cells by secreting toxins and utilise them as a nutrient [172]. It is the process of phenotypic differentiation that allows the bacterial colony to optimise its resources and stay resistant to harsh environmental condition.

Many of the details of the genetic circuits controlling these different cell states are understood at the single-cell level [34]. Conventional techniques for monitoring phenotypes in growing *B. Subtilis* biofilms include flow cytometry and fluorescent microscopy, using bacterial strains with fluorescent reporters for one or two phenotypes [34,173–178]. By tagging fluorescently one or two cell types at a time [34,179,180] it is possible to understand fully biofilm evolution. Wang et al. [181] developed a non-destructive method to analyse bacterial biofilm growth of a triple-labelled *B. Subtilis* strain, using optical transmission and fluorescence microscopy. This method made it possible to observe the spatial and temporal distribution of cell states, as well as that of low-fluorescent or non-fluorescent materials. The latter consists of the extracellular matrix and/or cells that are either dead or have decreased fluorescent expression levels [181], as shown in Figs. 23 and 24.

2.7. Wrinkle pattern evolution in B. Subtilis biofilms

Soft tissues in organisms tend to lose stability as a result of environmental changes and external incentives, which gives rise to a continuous evolution of surface wrinkling and morphology as the colony grows. This phenomenon has been observed both in vivo and in vitro. Additionally, different cell phenotypes can produce different wrinkle geometries, examples of which are the convoluted bowel [182] and cerebral cortex [183]. It is the heterogeneous growth of cell populations in organisms which dictates the evolution of their surface morphology and structure. There are well known examples from different growth phenomena: the edge of a leaf grows faster than the centre, generating residual stresses that can cause waviness at the edge [184,185]; the decay (or atrophy or lesions) of fruits and flowers drives to formation of irregular morphology [186–188]. Similar mechanisms affect the morphology of bacterial biofilms. The formation mechanism and physiological function of the biofilm morphology have been explored extensively in recent years. Experimental observations demonstrate that a network of folds can be generated in biofilms, creating water channels that facilitate material exchange between the internal parts of the biofilm and the environment [189,190]. Such a channel is shown in Fig. 25A. An important determinant of the complex morphology and structure of biofilms is cell differentiations into different phenotypes, which results in a heterogeneous population [191,192]. The non-uniform cell proliferation induces local stress gradients in biofilms, giving rise to mechanical instabilities that affect significantly surface wrinkling and interface delamination [193,194]. Another important morphology-driving mechanism is the withering and death of cells in the central area of the biofilm. When such cells stop functioning the stress around them is released to an extent. This leads to formation of irregular wrinkles around the centre of the biofilm [195], as shown in Figs. 25B-25D. Evolution and wrinkle formation can induce morphological transitions that, in turn, can shape further the biofilm dynamically changing morphology. The morphological transition is an irreversible phase transition [196–199] in that it leaves behind a fixed morphology that cannot be changed.

Rich morphological patterns were also found during the growth of triple fluorescent labelled *B. Subtilis* strains on MSgg agar substrate over 20 days [200–202]. The patterns included branches, labyrinthine networks, radial ridges, concentric rings and more. Similar results, including further morphologies were reported in [203] and are shown in Fig. 26A. Interesting are the morphological transitions of the wrinkle pattern during the growth. It underwent five successive evolutions from the biofilm centre to its edge: chaotic concentric rings (I), labyrinthine networks (II), radial ridges (III), branches (IV), and burgeons (V). The dynamics giving rise to these morphologies are varied. The wrinkle patterns I and II were shown to be caused by cell death in the centre of the biofilm, while the branching in IV (Fig. 26B)

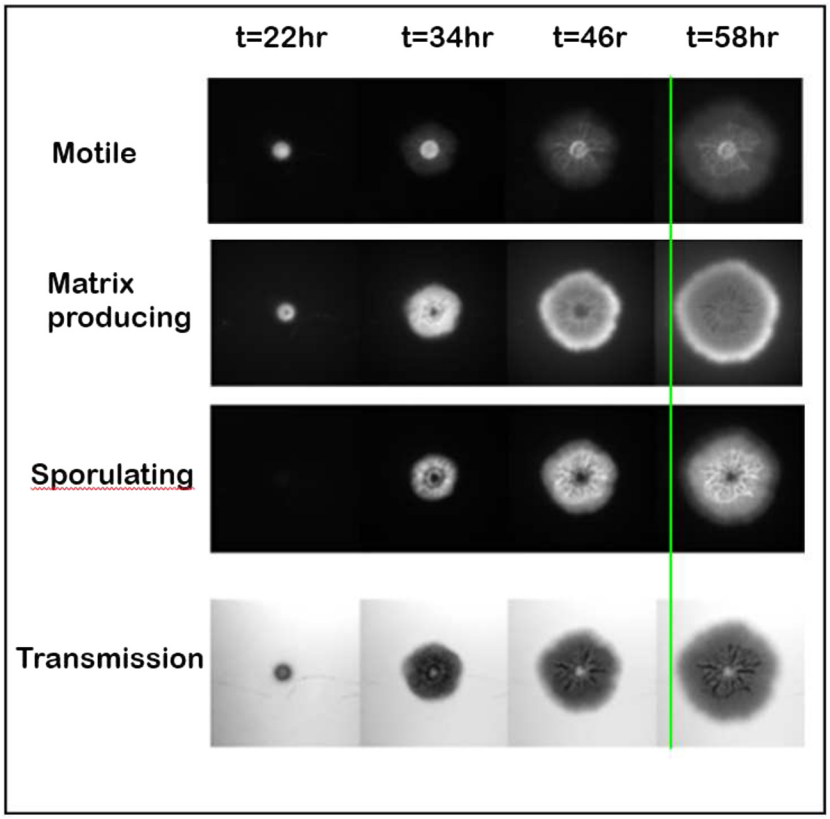

Fig. 23. Time-lapse images of a growing *B. Subtilis* biofilm. Time-lapse images of a growing *B. Subtilis* biofilm at t = 22 h, 34 h, 46 h, and 58 h after inoculation. When excited, the motile, matrix-producing and sporulating phenotypes produce different fluorescent colours and are observed using red, blue, and yellow filters, respectively. Transmission images are shown at the bottom and are used to determine the optical density. The green line serves as guide, indicating that at 58 h, the extent of the matrix-producing cells is comparable to that of the motile cells and exceeds that of the sporulating cells.

resulted directly from the wrinkle morphology in III and can be regarded as inherited from it. Similarly, the evolution into the complexity of the branching in V was a result of the patterning in IV. An example, shown in Fig. 26C, is of a wrinkle dividing into more than three branches. Beyond visual observations, measurements of wrinkle thickness and width in different regions showed systematic trends: radial wrinkles in III were the thickest and widest, with these decreasing steadily with the transitions into stages IV and V. This decrease was accompanied by an increase in the density of wrinkles, as shown in Figs. 26D and 26E.

Analysis in [203] of the phenotype distributions through the fluorescent intensity also revealed systematic patterns. Spores population outnumbered motile and matrix-producing cells in regions III and IV, but spores were in the minority in region V (Fig. 26G). The spores population was positively correlated with surface complexity (Fig. 26F), which the latter defined as the ratio of the biofilm's surface area, in contact with the air, to the projection of this area onto the plane.

A noticeable distinctive boundary between the radial ridge pattern and the dendritic pattern [203] has been attributed to interface instability, in which protrusions in a growing surface are prone to grow even faster, generating fingering phenomena, often leading to fractal patterns [204–206]. In the biofilm, the interface's instability resulted from slightly anisotropic local growth generating accumulation of residual stresses within the biofilm [207]. This is in contrast to other pattern evolution dynamics in the biofilm, where the evolution is gradual through a region. The evolution across boundaries is causal - from the radial ridge pattern to the dendritic pattern and then to the burgeon pattern. A similar pattern can be seen in bifurcated branches and lungs. Intriguingly, each biofilm pattern corresponds to different cell differentiation and growth rate. Specifically, when the growth state and internal stress of the phenotype

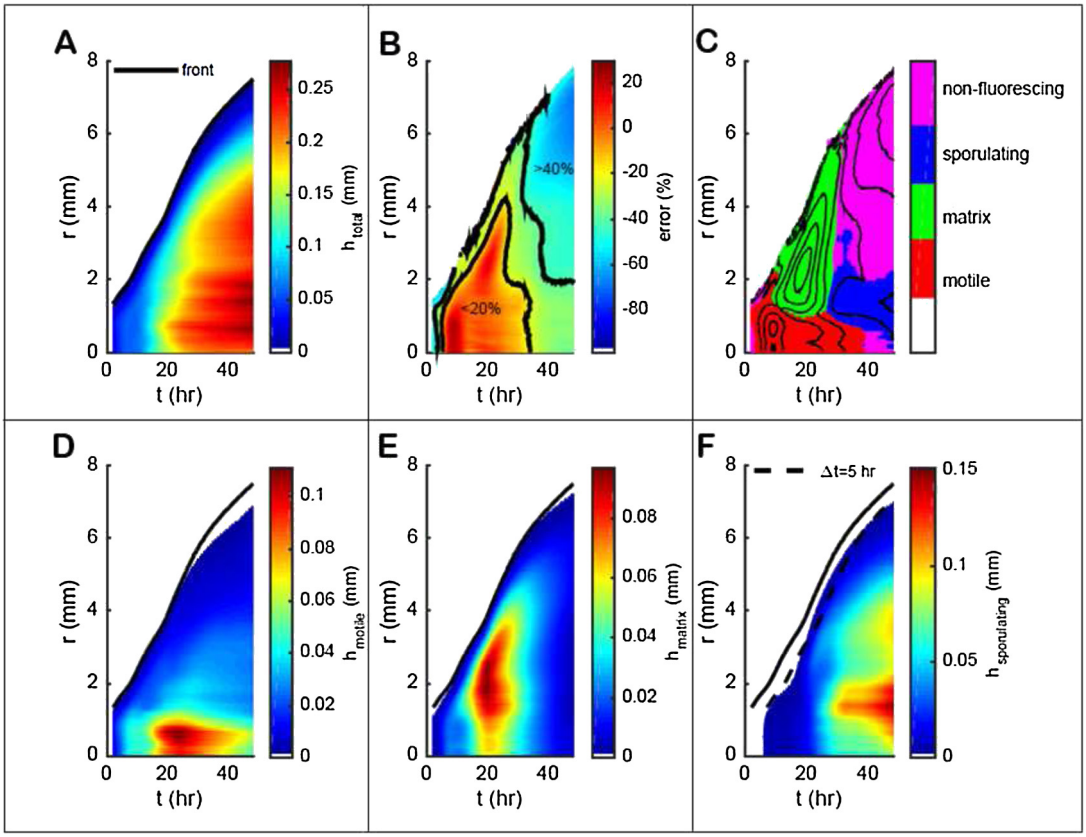

Fig. 24. Biofilm characteristics, averaged over the azimuthal angle, as functions of the distance from the centre, r, and time, t. **A.** The height of the biofilm as a whole, deduced from the optical density. **B.** The difference between the heights deduced from the optical density measurements and from fluorescent intensities of multiple channels, presumably because of excessive low-fluorescent and/or non-fluorescent materials. C. The phenotype majority and fluorescence spatial distribution in the biofilm. D–F. The height of the biofilm in the regions populated by the different phenotypes: motile, matrix producing, and sporulating cells. The full black line in A, D, E, and F indicates the size of the biofilm as a function of time. The dashed black line shows the points in time and space where the substrate has been colonised for 5 hours.

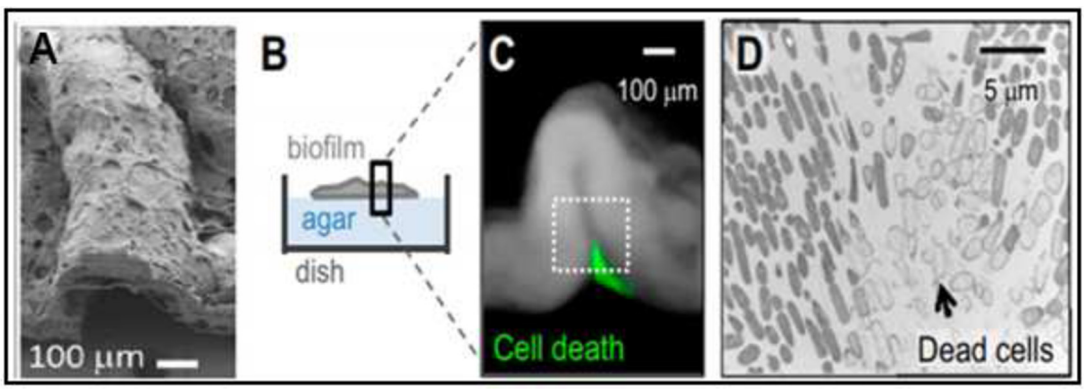

Fig. 25. The wrinkles in biofilm structure correlate with concentrations of dead cells. A. A water channel formed under a biofilm wrinkle. B. Sketch of the biofilm as viewed from the microscope for the fluorescence and bright-field imaging of a biofilm (in grey). Dashed lines indicate the direction of observation. C. Cross-section of an artificially coloured florescence image of a 30 h-old biofilm wrinkle. The PftsAZ-CFP is in grey and the cell death reporter Sytox is in green. D. A transmission electron microscope image of dead cells (black arrow) within the section of a biofilm wrinkle taken within the white box in C.

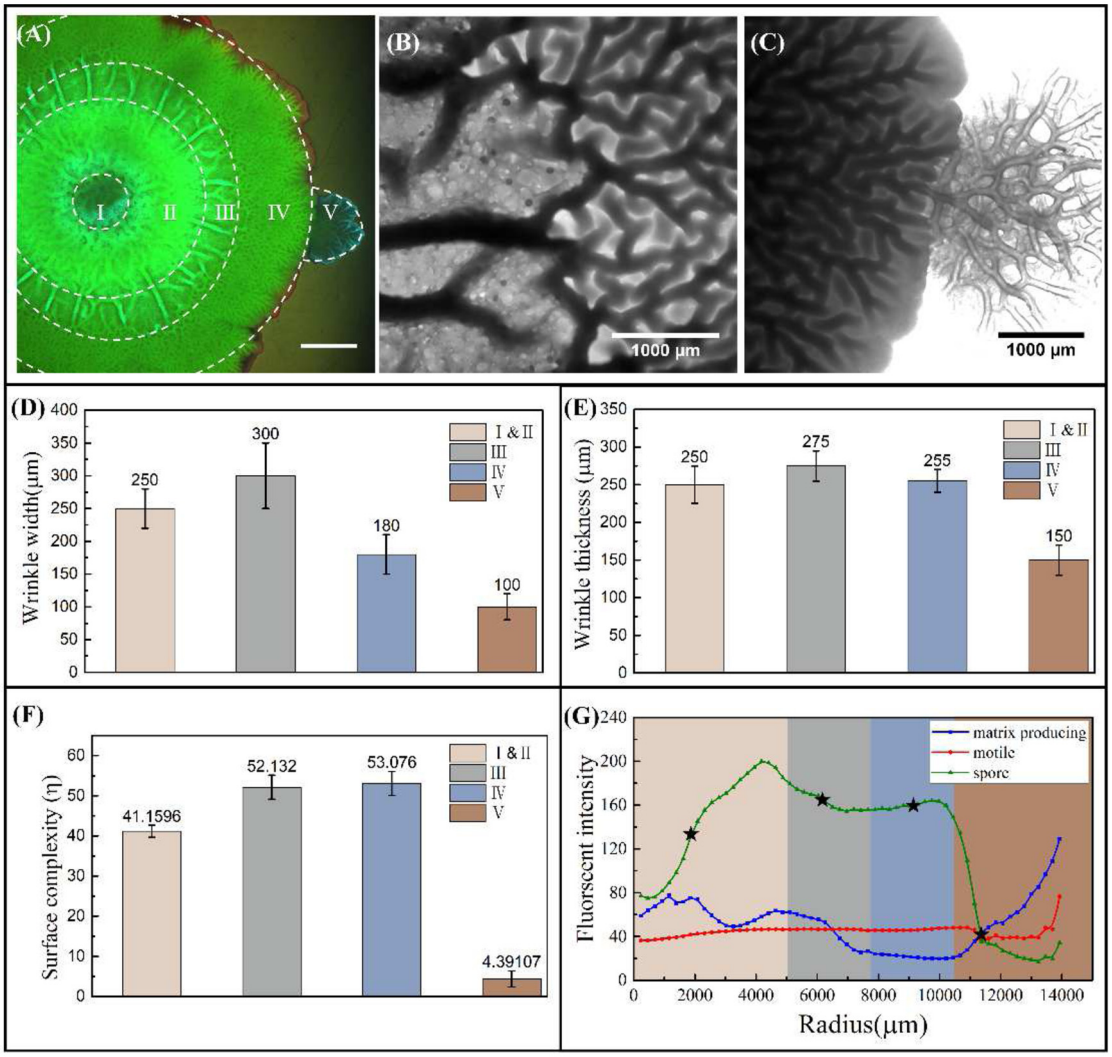

Fig. 26. Structural patterning and parameters of the wild type 3610 *B. Subtilis* biofilm, grown on MSgg agar substrate. The structural patterning of the wild type 3610 *B. Subtilis* biofilm, grown on MSgg agar substrate for 21 days. A. The wrinkle pattern undergoes five morphological transitions from the biofilm centre outwards: chaotic concentric rings (I), labyrinthine networks (II), radial ridges (III), branches (IV), and burgeons (V). The green colour represents spores, blue the matrix producing cells, and red the motile cells. The scale bar is 3 mm. B. Magnification of the transition region of the wrinkle pattern from III to IV. C. Magnification of the transition region of the pattern from IV to V. D. The wrinkle width in the five regions. E. The wrinkle thickness in the five regions. F. Surface complexities of five regions. The surface complexity is quantified by the ratio of the biofilm surface area in contact with the air to the projected area of the biofilm on the plane. G. The variation in the fluorescence intensities of different phenotypes as a function of distance from the centre [34].

reach a certain threshold, the morphology undergoes a transition. These transitions determine the interface evolution of the biofilm [208,209].

The morphology is also very sensitive to environmental conditions, including nutrient concentration and temperature. Analyses to determine the effects of these factors, as well as of the type of mutant, eps or flagellar, on the structural patterns, were carried out in [203]. Increasing agar concentration from 1.5 wt% to 2.0 wt%, was found to cause earlier formation of radial ridge wrinkles and branches, and a significant increase in biofilm surface complexity. Increasing the agar concentration further to 2.5 wt% revealed a domino effect: while not increasing the surface complexity (see Figs. 27A and 27C), this made the substrate harder. This hardening reduced the rate of water and nutrients absorption in cells, thereby accelerating the differentiation of matrix-producing cells into spores. The increase in spores population then increased rapidly the surface area, giving rise to wrinkles.

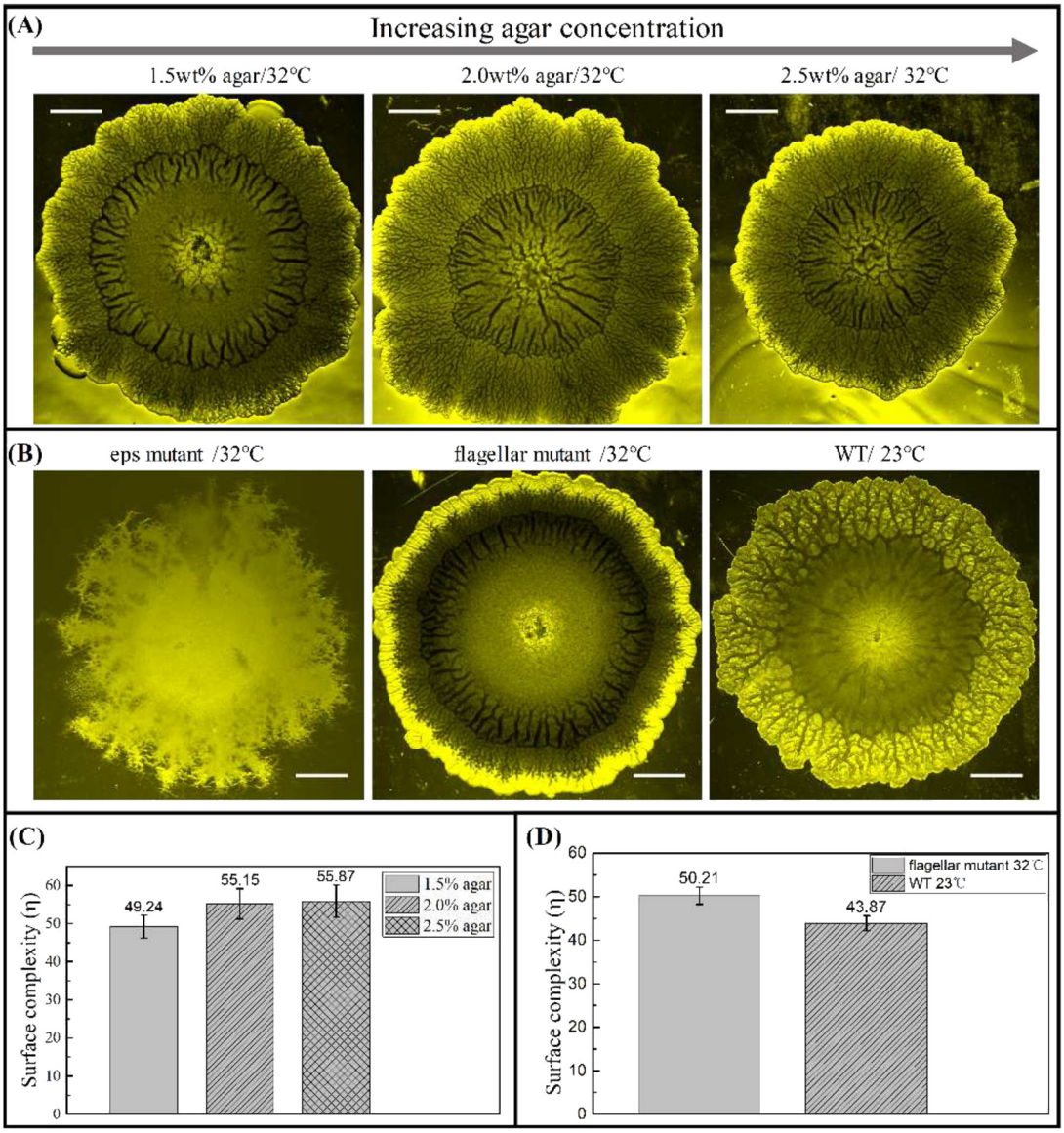

Fig. 27. Surface morphologies of 14 days old WT and mutant *B. Subtilis* biofilms in several environments. A. Surface morphologies of 14 days old WT *B. Subtilis* biofilms, grown on substrates with agar concentration of 1.5 wt%, 2.0 wt%, and 2.5 wt%, respectively. B. Surface morphologies of eps-mutant, flagellar mutant, and WT at the given temperatures. C-D. Average surface complexities of biofilms in A. and B. All scale bars are 3 mm.

The structural patterning was also found to depend strongly on the species: eps mutant *B. Subtilis* strains failed to form biofilms, as shown in Fig. 27B, while biofilm morphologies generated by wild-type *B. Subtilis* and flagellar mutants exhibited similar surface complexities, as shown in Fig. 27D.

The temperature-dependence of the biofilm morphology was studied in [203] by culturing biofilms at two different temperatures, 23 °C and 32 °C. A typical difference is shown in Fig. 27B - the patterning is more distinct and tighter at the higher temperature.

2.8. Collective cell motion patterns evolving in B.Subtilis biofilms

Biofilms fit well into the definition of complex systems [210,211] because their evolution is strongly constrained by the large number of cells in the biofilm and by the need to exchange chemical information both among cells and be-

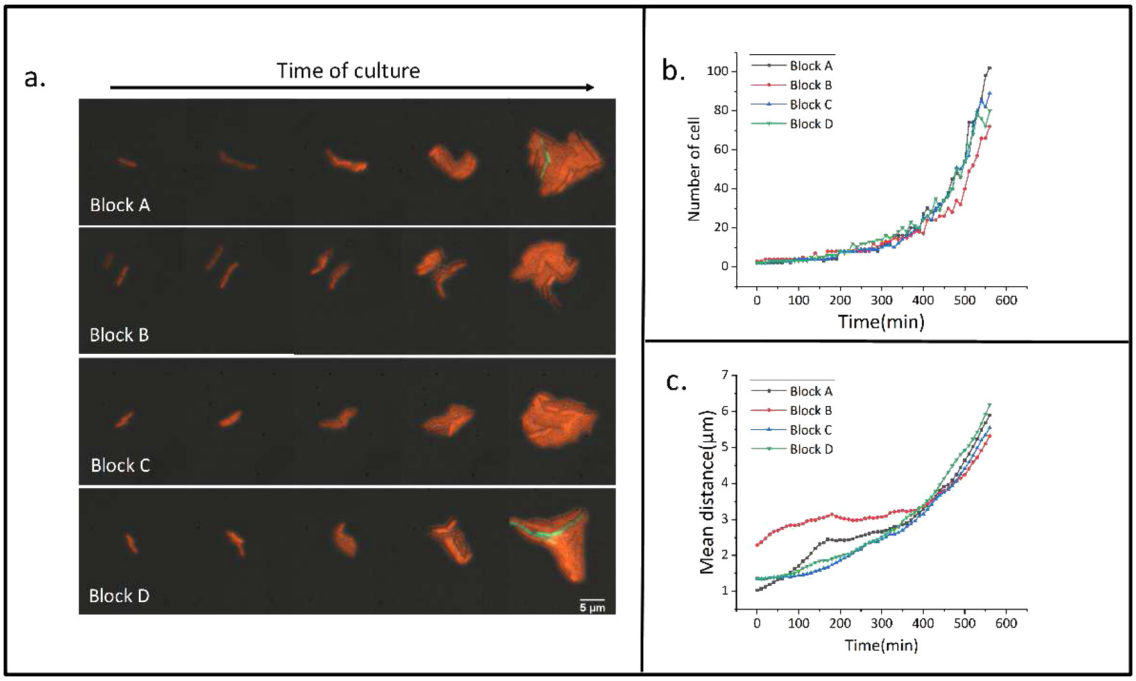

Fig. 28. Early growth of bacterial biofilms. **a.** Four bacterial colonies at the early growth stage. Blocks B and C contain only motile cells (coloured red), whilst in blocks A and D there emerge matrix-producing cells at the later time (coloured green). **b.** The time-dependence of the cell numbers in the four blocks. **c.** The time-dependence of the mean distance in the four blocks.

tween cells and the environment [212,213]. Indeed, many complex systems, made of elementary units, self-organise into distinct patterns. Examples abound in nature: snowflakes, desert dunes, diffusion-limited aggregates, viscous fingering, and many more. The global patterning is an emerging property of seemingly random but cooperative dynamics on the element-scale. The cooperativity is dictated by the inter-element interactions, which can be widely varied [214–218]. In biofilms, these interactions are governed by the aforementioned constraints, which determine cell proliferation, mechanical interactions, and information exchange [219,220].

During the growth of *B. Subtilis* biofilm, to cope with diverse environments, cells differentiate into the different phenotypes - motile cells, matrix-producing cells, and spores [34,221]. These phenotypes differ in their adhesion, motility, and shape characteristics, and their inter-phenotype interactions govern the emergent diverse biofilm structures [222,223]. In a recent study [224], it was found that motile cells tend to be compact within few hours of the initial inoculation before matrix-producing cells appear. The matrix-producing cells then form elongated structures that interfere with tendency of motile cells to form rounded ones. This is a structure-mediated interaction between the motile and matrix-producing cells, forcing the former to grow within the boundaries forced by the latter. This process is illustrated in Fig. 28. After ten hours of inoculation, some colonies tend to be compact and only have motile cells, seen in Fig. 28a Blocks B and C (in red), while others appear more oriented (Fig. 28a Blocks A and D) because of the directional influence of the chain-like structure of the matrix-producing cells (in green) on the colony's expansion.

To quantify the structural analysis, we must consider the energetic barriers to growth in different directions, as different cell types deal with these barriers differently. The energetics of the growth dynamics depend on the cell types, sizes, numbers, and the inter-cellular interactions. The energy barrier to overcome during growth can be written in the form

$$E = \sum_{i=1}^{n} \left(\int_0^{d_i} F_i dl + \int_0^{\theta_i} M_i d\theta \right), \tag{1}$$

in which the sum is over all the n cells, F_i is the frictional resistance to the ith cell when it deviates from the centre of the population, d_i is the cell's distance from the centre of the colony, θ_i is the angle between the long axis of the ith

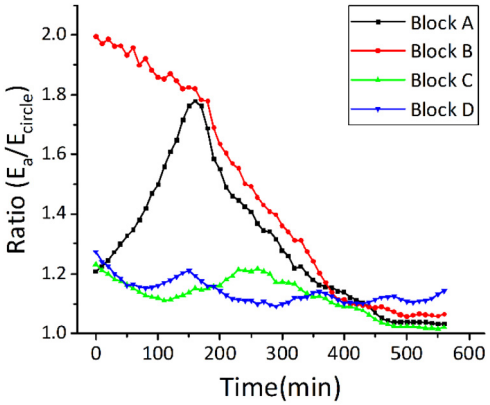

Fig. 29. The time-dependence of the energy-based shape parameters. The time-dependence of the colonies' energy-based shape parameters, E_{block}/E_{circle}, normalised by the uniform circle's energy barrier, defined in eq. (2).

cell and d_i, and M_i is the resistance moment to the ith cell being deflected from this angle. For a uniform circle with no angular preference,

$$E_{circle} = \int_0^R \sigma r 2\pi r dr = \frac{2\pi R^3 \sigma}{3}. \tag{2}$$

There are several ways to characterise a colony's shape. We define the mean cell distance as the average distance between the cell positions and the colony's centre, $|r_{cell} - r_0|$, measured in either pixels or μm,

$$\overline{r} \equiv \frac{\sum_{cells} |r_{cell} - r_0| a}{Colony\ area}, \tag{3}$$

in which a is an individual cell's area and the colony's centre is defined as

$$r_0 \equiv \frac{\sum_{cells} r_{cell}}{Number\ of\ cells}. \tag{4}$$

Neglecting buckling out of the plane, the shapes range from the most compact one - the circle - to the most stretched one - the line. For these extremes the mean distances are:

$$\overline{r}_{circle} = \frac{1}{\pi R^2} \int_0^R r 2\pi r dr = \frac{2}{3} R \tag{5a}$$

$$\overline{r}_{line} = \frac{2}{L} \int_0^{L/2} r dr = \frac{1}{4} L, \tag{5b}$$

in which R and L are the circle's radius and the line's length, respectively. For illustration, consider a linear and a circular single-phenotype colonies, each of $N = 2^{t/\tau}$ cells, with t time and τ the mean division period. The areas of both colonies are Na. Their mean distances are

$$\overline{r}_{circle} = \frac{2}{3}\sqrt{\frac{a}{\pi}} 2^{t/2\tau} = \frac{2}{3}\sqrt{\frac{aN}{\pi}} \tag{6a}$$

$$\overline{r}_{line} = \frac{\sqrt{a}}{4} 2^{t/\tau} = \frac{\sqrt{a}}{4} N. \tag{6b}$$

The situation is slightly more complicated in multi-phenotype colonies, both because each phenotype has a different growth pattern and because the phenotypes divide preferentially at different stages of the colony's evolution.

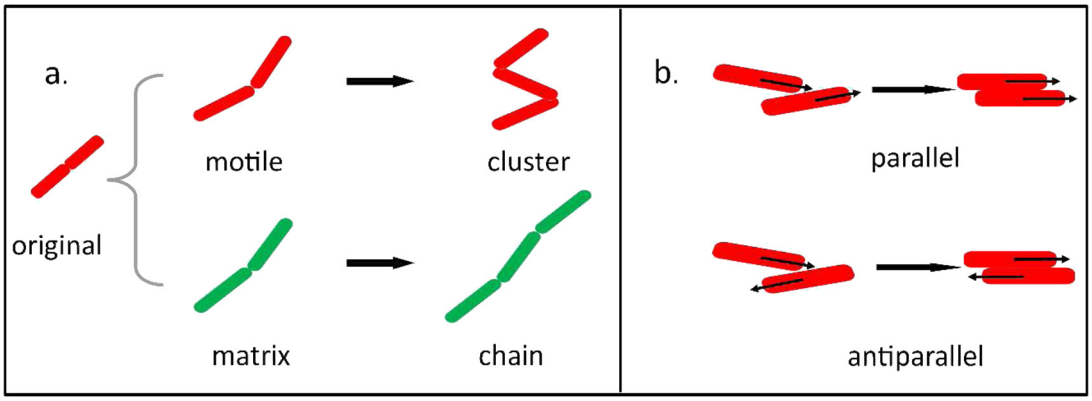

Fig. 30. Characteristics of single-cell movement. **a.** During cell divisions, the mother cell grows and elongates and divides when the cell reaches its maximum length. After division, the long axes of the mother cell and the daughter cell are oriented similarly up to small deviations. **b.** Parallel and antiparallel configurations.

In the growth of *B. Subtilis* biofilms, the time-dependence of the cell numbers and the mean distances are shown in Figs. 29b and 29c, respectively. The growth pattern of block B differs from the other three, most pronouncedly between t=200 min and t=400 min, when the colony grows but the mean distance hardly changes. This is a result of the separation into two sub-colonies in this block, which affects directly the mean distance. This establishes that the mean distance is a useful descriptor of the shape. Beyond $t = 450$ min, the growth rates are similar in all the blocks, as is reflected by the shapes shown in Fig. 29a, with all the colonies being roughly compact. It is noteworthy that at this stage there are fewer cells in block B (Fig. 29b) than in the other blocks and that the cell number ratios, e.g., N_A/N_B, increases faster than the ratio $\overline{r}_A/\overline{r}_B$. This is because the mean distance grows as $\sqrt{N}$ in compact clusters, as eq. (6a) shows. The increase with time of cell number ratios is the result of the emergence of matrix-producing cells, which tend to form elongated structures and bias the expansion towards the directional and line-like. The transition from a directional growth to compact is best seen in block A around $t = 150$ min, when the mean distance's growth changes from being proportional to N to being proportional to $\sqrt{N}$. This transition is also clearly observed in the time-dependence of the energy barrier, shown in Fig. 29.

The large number of cells of each phenotype in the biofilm and their seemingly random movements [225] makes it impractical to describe the dynamics on the cell-scale. 'Macroscopic' dynamic models of colony shape evolutions are then more useful. To bridge between the cell and the colony scales, Wolfram [226] adopted a methodology that is common in analysing inanimate complex systems. The first step is to generalise key characteristics of single-cell movement, as follows:

(i) The driving force for the cell movement is its elongation and proliferation.
(ii) After division, the orientation of the long axis of the daughter cell is correlated strongly with that of the mother cell, as illustrated in Fig. 30a. This correlation is higher in matrix-producing cells than in motile cells, which is the cause for the former forming elongated structures. However, too high correlations, resulting in almost exact orientations, lead to breakage of cell bonds.
(iii) Adjacent non-mother-daughter cells can be either parallel or antiparallel, as illustrated in Fig. 30b.

The compactness of the colony at the late stage of the colony's evolution is determined to a large extent by the interplay between characteristics (ii) and (iii).

Using this methodology to analyse experimental images, Olfati-Saber [227] and Reynolds [228] obtained relations between key characteristics of single-cell movement and colony shapes. They also constructed a multi-agent model, which was implemented in a numerical simulation, in which cells were modelled as single particles (agents). Simulating agents that behave only as motile cells, i.e., with a predetermined angle between the orientations of mothers and daughters, indeed gave rise to compact colonies. Simulating colonies of the two phenotypes, the motile cells arrays changed from compact to expansion along the chain-like directions of matrix-producing cells. The experimental observations suggested that colony growth along the chain direction lasts several hours after the appearance of matrix-

producing cells. However, as the matrix-producing cells proliferate, the colony reverts to the compact structure. This is because of two effects. One is that too long chain structures are unstable and tend to break or bend significantly. Another is that matrix-producing cells 'nucleate' in a number of locations, with chain directions oriented randomly in each location. These then interfere with one another as the chains elongate, disrupting the directional correlations.

3. Concluding remarks

A number of experimental measurements and computational techniques have been developed to investigate the complex cooperative behaviour of bacteria [229–231]. Despite the great progresses described above, there is still no fundamental theoretical and predictive modelling of the dynamics of biofilm evolution. One difficulty is the difficulty to obtain reliable data on local parameters [232] and one way around this problem is to adopt a more physics-based approach and shift the focus from the local to the larger-scale picture by modelling 'coarse-grained' properties and behaviour. It is only on larger length-scales and longer time-scales that the self-organisation [233] of these systems become apparent. Introduced in 1987, self-organised criticality is a pattern of behaviour that many dynamical out-of-equilibrium systems share. By definition, self-organised states are of low-entropy, in contrast to entropy-maximising equilibrium systems. The ordered phase in such systems is often quantified by an 'order parameter' and the entropy is a measure of the system's disorder. In spite of the contrast in the entropic behaviour, the characteristic approach to self-organised criticality is similar to the way equilibrium systems approach second-order phase transitions and critical points. Additionally, phase transitions in inanimate system are characterised by 'collective behaviour' [234], in which the behaviour of far-away micro-scale units is correlated in spite of the fact that the interactions are short-range on the unit scale. Such a collective behaviour, correlated over distances larger than a few bacteria, is also prevalent in biofilms. This similarity, combined with the large body of existing knowledge on behaviour in the vicinity of critical points, can be used to develop a new generation of predictive models for the evolving morphology of biofilms. Moreover, many inanimate physical systems, of widely different microscale properties, approach a phase transition along the same route, often with an identical divergence of the correlation length. Such systems are said to be in the same 'universality class'. This means that the details of the evolving morphology are blurred out and only coarse-grained parameters are important to model the process of the growth of the correlation length. It is then possible that the modelling of such phenomena in inanimate systems, of which there are many examples, could be a promising way towards predictive modelling in bacterial biofilms. In particular, existing models of potential systems in the same universality class could be adapted. Nevertheless, unlike physical systems, biological ones may have many states (or 'phases'), each of which characterisable by a specific order parameter, such as network activity, large-scale low expression genes, and a range of structural descriptors [235,236]. Examples of the latter include curvature and twist to describe transitions of the bacterial flagellar filament. Order parameters need not be scalar – they could be vectors or tensors. Indeed, tensors are often used to describe structures quantitatively [20,237]. Conceptually, modelling many-phase systems is no different than few-phase ones, but the behaviour would most likely be richer and more complex, not least because of the different order parameters of different phases.

Adaptation of physical models of phase transitions to emergent phenomena in bacterial biofilm has started to attract attention. Several examples are the following. You et al. [238] demonstrated that a mono-to-multi-layer transition in growing bacterial colonies is driven by a competition between growth-induced in-plane active stresses and vertical restoring forces resulting from cell-substrate interactions. The transition sets in when individual cells become unstable to rotations. Modelling cell division as a Poison process and defining the Poisson process rate as an order parameter, they showed that the transition from monolayers to multilayered structures can be described as a continuous phase transition. Depletion-induced phase separations have also been observed in biofilms, both on solid substrates and in fluid environments [239–245]. The order parameter Q6 can be used to distinguish between liquid-like disorder, in which Q6=0, and solid-like order, in which Q6=1 [246]. Ghosh et al. [247] showed that the typical value of Q6 increases significantly with depletion. This was then explained as the result of mechanically driven depletion inducing cell ordering as the biofilms grow on the solid substrates. Zhai et al. [248] discovered recently that the long-range propagation of electrical signals in biofilms of *B. Subtilis* can be modelled by an extended version of the classical percolation theory [249]. While in the standard theory, sites are on or off independent from one another, they found that the probability of a cell to signal is correlated with its nearest neighbours. They then extended the classical model to describe correlated percolation of signalling, driven cell division, phenotypic inheritance, and cell displacement. The order parameter, which they define, is then the difference between the probability of a cell to be on when the cell

above it is on and when the cell above it is off. The observation of these correlations encouraged Zhai et al. to use nearest-neighbour interacting spin models to describe the signal propagation phenomenon, a direction that would be interesting to continue exploring. Dell'Arciprete et al. [250] used the physics-based formalism of liquid crystals to model the structural evolution of growing two-dimensional colonies of rod-shaped *E. Coli*. They focus on 'topological charges' that appear during the growth, which are points where the directional orientation order parameter is singular. Using analytical tools commonly employed in analyses of phase transitions, they show that the colonies self-organise into a scale-invariant structure. This places those structures in a universality class that is different from conventional active nematic liquid crystals. The main significance of that work is not as much in understanding the particular phenomenon they studied but rather in the attempt to describe the large-scale dynamics with continuum dynamic equations that are characteristic to many fields in physics, from the atomic to the cosmological scales. Hartmann et al. [251] combined experimental and theoretical analyses to show that the emergence of local nematic order in growing V. Cholerae biofilms can be captured by an effective cell–cell interaction potential, thus translating molecular mechanisms into force parameters. Although the potential they used is unlike any other in conventional physical systems, it appears to describe reasonably well the global behaviour of a liquid-crystalline-like colony of about 10,000 individual bacteria.

These examples suggest that bridging between the cell-scale and coarse-grained continuum descriptions could benefit greatly the understanding global behaviour of biofilms. In particular, this can lead to advances in modelling transitions between different morphological and growth states. The quest for such a bridging is the main approach in physics, where the default modelling of most physical systems is often in the continuum. Turning to physics-based models in general, and to descriptions of phase transitions in particular, to gain insight into large-scale dynamics and self-organisation of biofilms, is a promising emerging approach. Nevertheless, going down this route should be done with caution. This is because physics models often comprise simplified versions of the real systems and the skills of a physicist are to reduce a system to the smallest number of significant mechanisms and variables. While this approach has been extremely useful in modelling inanimate systems, biofilms and active matter are quite complex and often cannot be reduced to a few-parameters modelling. The reason is that active matter can adapt to changing circumstances and environments by changing the behaviour both on the intra-cellular level, as well as manipulate inter-cellular interactions. While this makes the dynamics of richer, it also means that the models need also be adaptable and more versatile than in conventional physics.

CRediT authorship contribution statement

The authors contributed equally to all aspects of the article.

Declaration of competing interest

The authors declare that they have no known competing financial interests or personal relationships that could have appeared to influence the work reported in this paper.

Acknowledgements

XW acknowledges the support of the NSFC, Grants: 11772047, 11972074, 11620101001. RB acknowledges the hospitality of the Cavendish Laboratory, University of Cambridge. XF acknowledges the support of NSFC (11620101001 and 11921002).

References

[1] Landau L, Lifshitz E. Theory of elasticity. Pergamon Press; 1986.
[2] Cahn JW, Hilliard JE. Free energy of a nonuniform system. I. Interfacial free energy. J Chem Phys 1958;28:258–67.
[3] Mindlin RD. Second gradient of strain and surface-tension in linear elasticity. Int J Solids Struct 1965;1:417–38.
[4] Triantafyllidis N, Bardenhagen S. On higher order gradient continuum theories in 1-D nonlinear elasticity. Derivation from and comparison to the corresponding discrete models. J Elast 1993;33:259–93.
[5] Beysens DA, Glazier JA Forgacs G. Cell sorting is analogous to phase ordering in fluids. Proc Natl Acad Sci USA 2000;97:9467–71.

[6] Pérez-Pomares JM, Foty RA. Tissue fusion and cell sorting in embryonic development and disease: biomedical implications. BioEssays 2006;28:809–21.
[7] Revell C, Blumenfeld R, Chalut KJ. Force-based three-dimensional model predicts mechanical drivers of cell sorting. Proc R Soc B, Biol Sci 2019;286:20182495.
[8] Bak P, Bhattacharya S. How nature works: the science of self-organized criticality. Phys Today 1997;50:71–2.
[9] Strick TR, Allemand JF, Bensimon D, Croquette V. Stress-induced structural transitions in DNA and proteins. Annu Rev Biophys Biomol Struct 2000;29:523–43.
[10] Smith SB, Cui Y, Bustamante C. Overstretching B-DNA: the elastic response of individual double-stranded and single-stranded DNA. Science 1996;271:795–9.
[11] Clausen-Schaumann H, Rief M, Tolksdorf C, Gaub HE. Mechanical stability of single DNA molecules. Biophys J 2000;78:1997–2007.
[12] Ahsan A, Rudnick J, Bruinsma R. Elasticity theory of the B-DNA to S-DNA transition. Biophys J 1998;74:132–7.
[13] Cluzel P, Lebrun A, Heller C, Lavery R, Viovy JL, Chatenay D, et al. DNA an extensible molecule. Science 1996;271:792–4.
[14] Konrad MW, Bolonick JI. Molecular dynamics simulation of DNA stretching is consistent with the tension observed for extension and strand separation and predicts a novel ladder structure. J Am Chem Soc 1996;118:10989–94.
[15] Olson GB, Hartman H. Martensite and life: displacive transformations as biological processes. J Phys, Colloq 1982;43:855–65.
[16] Harris WF, Scriven LE. Cylindrical crystals, contractile mechanisms of bacteriophages and the possible role of dislocations in contraction. J Theor Biol 1970;27:233–57.
[17] Klug L. Three-dimensional image reconstructions of the contractile tail of T4 bacteriophage. J Mol Biol 1975;99:51–64.
[18] Moody MF. Sheath of bacteriophage T4: III. Contraction mechanism deduced from partially contracted sheaths. J Mol Biol 1973;80:613–35.
[19] Moody MF. Structure of the sheath of bacteriophage T4. II. Rearrangement of the sheath subunits during contraction. J Mol Biol 1967;25:201–8.
[20] Ciamarra MP. Comment on "Granular entropy: Explicit calculations for planar assemblies". Phys Rev Lett 2007;99:089401.
[21] Blumenfeld R, Amitai S, Jordan JF, Hihinashvili R. Failure of the volume function in granular statistical mechanics and an alternative formulation. Phys Rev Lett 2016;116:148001.
[22] Sun X, Kob W, Blumenfeld R, Tong H, Wang Y, Zhang J. Friction-controlled entropy-stability competition in granular systems. Phys Rev Lett 2020;125:268005.
[23] Olson GB. New directions in martensite theory. Mater Sci Eng A 1999;273:11–20.
[24] Gang B. Mechanics of biomolecules. J Mech Phys Solids 2002;50:2237–74.
[25] Vliet K, Bao G, Suresh S. The biomechanics toolbox: experimental approaches for living cells and biomolecules. Acta Mater 2003;51:5881–905.
[26] Ehrenberg CG. Die infusionsthierchen als vollkommene organismen. Ein blick in das tiefere organische leben der natur. Leipzig: L. Voss; 1838.
[27] Bardy SL, Ng SYM, Jarrell KF. Prokaryotic motility structures. Microbiology 2003;149:295–304.
[28] Friesen JD. Escherichia coli and salmonella cellular and molecular biology. Science 1998;240:1678–81.
[29] Samatey FA, Imada K, Nagashima S, et al. Structure of the bacterial flagellar protofilament and implications for a switch for supercoiling. Nature 2001;410:331–7.
[30] Morgan DG, Khan S. Bacterial flagella. Berlin, Heidelberg: Springer; 2001.
[31] Turner L, Ryu WS, Berg HC. Real-time imaging of fluorescent flagellar filaments. J Bacteriol 2000;182:2793–801.
[32] Cecile B, Ellison CK, Adrien D, Brun YV. Bacterial adhesion at the single-cell level. Nat Rev Microbiol 2018;16:616–27.
[33] Vlamakis H, Chai Y, Beauregard P, Losick R, Kolter R. Sticking together: building a biofilm the Bacillus subtilis way. Nat Rev Microbiol 2013;11:157–68.
[34] Vlamakis H, Aguilar C, Losick R, Kolter R. Control of cell fate by the formation of an architecturally complex bacterial community. Genes Dev 2008;22:945–53.
[35] Zhang W, Seminara A, Suaris M, Brenner MP, Weitz DA, Angelini TE. Nutrient depletion in Bacillus subtilis biofilms triggers matrix production. New J Phys 2014;16:015028.
[36] Rumbaugh KP, Sauer K. Biofilm dispersion. Nat Rev Microbiol 2020;18:571–86.
[37] Serra DO, Hengge R. Cellulose in bacterial biofilms. In: Cohen E, Merzendorfer H, editors. Extracellular sugar-based biopolymers matrices. Cham: Springer International Publishing; 2019. p. 355–92.
[38] Berg HC. The rotary motor of bacterial flagella. Annu Rev Biochem 2003;72:19–54.
[39] Sowa Y, Berry RM. Bacterial flagellar motor. Tanpakushitsu Kakusan Koso 2008;41:103–32.
[40] Blair D. Bacterial flagellar motor: biochemical and structural studies. Berlin, Heidelberg: Springer; 2013.
[41] Kitao A, Hata H. Molecular dynamics simulation of bacterial flagella. Biophys Rev 2018;10:617–29.
[42] Khan S. The architectural dynamics of the bacterial flagellar motor switch. Biomolecules 2020;10:833.
[43] Gordon VD, Wang L. Bacterial mechanosensing: the force will be with you, always. J Cell Sci 2019;132:jcs227694.
[44] Minamino T, Kinoshita M, Namba K. Directional switching mechanism of the bacterial flagellar motor. Comput Struct Biotechnol J 2019;17:1075–81.
[45] Macnab RM. How bacteria assemble flagella. Annu Rev Microbiol 2003;57:77–100 [Review].
[46] Minamino T, Namba K. Self-assembly and type III protein export of the bacterial flagellum. J Mol Microbiol Biotechnol 2004;7:5–17.
[47] Minamino T, Imada K, Namba K. Molecular motors of the bacterial flagella. Curr Opin Struct Biol 2008;18:693–701.
[48] Francis NR, Sosinsky GE, Thomas D, et al. Isolation, characterization and structure of bacterial flagellar motors containing the switch complex. J Mol Biol 1994;235:1261–70.
[49] Suzuki H, Yonekura K, Namba K. Structure of the rotor of the bacterial flagellar motor revealed by electron cryomicroscopy and single-particle image analysis. J Mol Biol 2004;337:105–13.

[50] Thomas DR, Francis NR, Xu C, et al. The three-dimensional structure of the flagellar rotor from a clockwise-locked mutant of salmonella enterica Serovar typhimurium. J Bacteriol 2006;188:7039–48.
[51] Minamino T, Imada K. The bacterial flagellar motor and its structural diversity. Trends Microbiol 2015;23:267–74.
[52] Khan S, Macnab RM. The steady-state counterclockwise/clockwise ratio of bacterial flagellar motors is regulated by protonmotive force. J Mol Biol 1980;138:563–97.
[53] Elston TC, Oster G. Protein turbines. I: the bacterial flagellar motor. Biophys J 1997;73:703–21.
[54] Wadhams GH, Armitage JP. Making sense of it all: bacterial chemotaxis. Nat Rev Mol Cell Biol 2004;5:1024–37.
[55] Parkinson JS, Hazelbauer GL, Falke JJ. Signaling and sensory adaptation in Escherichia coli chemoreceptors: 2015 update. Trends Microbiol 2015;23:257–66.
[56] Lele PP, Branch RW, Nathan V, Berg HC. Mechanism for adaptive remodeling of the bacterial flagellar switch. Proc Natl Acad Sci USA 2012;109:20018–22.
[57] Delalez NJ, Berry RM, Armitage JP. Stoichiometry and turnover of the bacterial flagellar switch protein FliN. mBio 2014;5:e01216-14.
[58] Chang Y, Zhang K, Carroll BL, Zhao X, Charon NW, Norris SJ, et al. Molecular mechanism for rotational switching of the bacterial flagellar motor. Nat Struct Mol Biol 2020;27:1041–7.
[59] Scharf BE, Fahrner KA, Turner L, Berg HC. Control of direction of flagellar rotation in bacterialchemotaxis. Proc Natl Acad Sci USA 1998;95:201–6.
[60] Cluzel P, Surette M, Leibler S. An ultrasensitive bacterial motor revealed by monitoring signaling proteins in single cells. Science 2000;287:1652–5.
[61] Monod J, Wyman J, Changeux JP. On the nature of allosteric transitions: a plausible model. J Mol Biol 1965;12:88–118.
[62] Alon U, Camarena L, Surette MG, et al. Response regulator output in bacterial chemotaxis. EMBO J 2014;17:4238–48.
[63] Turner L, Samuel A, Stern AS, Berg HC. Temperature dependence of switching of the bacterial flagellar motor by the protein CheY. Biophys J 1999;77:597–603.
[64] Duke T, Novère N, Bray D. Conformational spread in a ring of proteins: a stochastic approach to allostery. J Mol Biol 2001;308:541–53.
[65] Korobkova EA, Emonet T, Park H, Cluzel P. Hidden stochastic nature of a single bacterial motor. Phys Rev Lett 2006;96:058105.
[66] Tu Y. The nonequilibrium mechanism for ultrasensitivity in a biological switch: sensing by Maxwell's demons. Proc Natl Acad Sci 2008;105:11737–41.
[67] Bai F, Branch RW, Nicolau DV, Pilizota T, Steel BC, Maini PK, et al. Conformational spread as a mechanism for cooperativity in the bacterial flagellar switch. Science 2010;327:685–9.
[68] Yuan J, Fahrner KA, Berg HC. Switching of the bacterial flagellar motor near zero load. Proc Natl Acad Sci USA 2014;390:394–400.
[69] Block SM, Segall JE, Berg HC. Adaptation kinetics in bacterial chemotaxis. J Bacteriol 1983;154:312–23.
[70] Korobkova E, Emonet T, Vilar J, Shimizu TS, Cluzel P. From molecular noise to behavioural variability in a single bacterium. Nature 2004;428:574–8.
[71] Wang F, Shi H, He R, Wang R, Zhang R, Yuan J. Non-equilibrium effect in the allosteric regulation of the bacterial flagellar switch. Nat Phys 2017;13:710–4.
[72] Matsuura S, Shioi JI, Imae Y, Iida S. Characterization of the Bacillus subtilis motile system driven by an artificially created proton motive force. J Bacteriol 1979;140:28–36.
[73] Shioi JI, Matsuura S, Imae Y. Quantitative measurements of proton motive force and motility in Bacillus subtilis. J Bacteriol 1980;144:891–7.
[74] Kojima S, Imada K, Sakuma M, Sudo Y, Namba K. Stator assembly and activation mechanism of the flagellar motor by the periplasmic region of MotB. Mol Microbiol 2010;73:710–8.
[75] Zhu S, Takao M, Li N, Sakuma M, Nishino Y, Homma M, et al. Conformational change in the periplamic region of the flagellar stator coupled with the assembly around the rotor. Proc Natl Acad Sci USA 2014;111:13523–8.
[76] Terahara N, Kodera N, Uchihashi T, Ando T, Minamino T. Na^+ -induced structural transition of MotPS for stator assembly of the Bacillus flagellar motor. Sci Adv 2017;3:eaao4119.
[77] Kojima S, Takao M, Almira G, Kawahara I, Sakuma M, Homma M, et al. The helix rearrangement in the periplasmic domain of the flagellar stator B subunit activates peptidoglycan binding and ion influx. Structure 2018;26:590–8.
[78] Sowa Y, Rowe A, Leake M, Yakushi T, Homma M, Ishijima A, et al. Direct observation of steps in rotation of the bacterial flagellar motor. Nature 2005;437:916–9.
[79] Ito KI, Nakamura S, Toyabe S. Cooperative stator assembly of bacterial flagellar motor for autonomous torque regulation. Nat Commun 2021;12(1):1–7.
[80] Nord AL, Gachon E, Perez-Carrasco R, Nirody JA, Barducci A, Berry RM, et al. Catch bond drives stator mechanosensitivity in the bacterial flagellar motor. Proc Natl Acad Sci 2017;114:12952–7.
[81] Wadhwa N, Phillips R, Berg HC. Torque-dependent remodeling of the bacterial flagellar motor. Proc Natl Acad Sci 2019;116:11764–9.
[82] Shi H, Ma S, Zhang R, Yuan J. A hidden state in the turnover of a functioning membrane protein complex. Sci Adv 2019;5:eaau6885.
[83] Friesen JD. Escherichia coli and salmonella: cellular and molecular biology. In: Neidhardt FC, editor, 2nd ed. Washington, D.C.: Science; 1998. p. 1678–81.
[84] Lowy J, Hanson J. Electron microscope studies of bacterial flagella. J Mol Biol 1965;11:293–313.
[85] O'Brien EJ, Bennett PM. Structure of straight flagella from a mutant salmonella. J Mol Biol 1972;70:133–52.
[86] Calladine CR. Construction of bacterial flagella. Nature 1975;255:121–4.
[87] Calladine CR. Design requirements for the construction of bacterial flagella. J Theor Biol 1976;2:469–89.
[88] Calldine CR. Change of waveform in bacterial flagella: the role of mechanics at the molecular level. J Mol Biol 1978;118:457–79.
[89] Yamashita I, Hasegawa K, Suzuki H, Vonderviszt F, Mimori-Kiyosue Y, Namba K. Structure and switching of bacterial flagellar filaments studied by X-ray fiber diffraction. Nat Struct Biol 1998;5:125–32.

[90] Yonekura K, Maki-Yonekura S, Namba K. Complete atomic model of the bacterial flagellar filament by electron cryomicroscopy. Nature 2003;424:643–50.
[91] Asakura S. Polymerization of flagellin und polymorphism of flagella. Adv Biophys 1970;1:99–155.
[92] Hotani H. Interconversion between flagella and P-filament in vitro. J Mol Biol 1971;57:575–87.
[93] Lowey S, Slayter HS, Weeds AG, Baker H. Substructure of the myosin molecule: I. Subfragments of myosin by enzymic degradation. J Mol Biol 1969;42:1–29.
[94] Hotani H. Light microscope study of mixed helices in reconstituted salmonella flagella. J Mol Biol 1976;106:151–66.
[95] Kamiya R, Asakura S. Helical transformations of salmonella flagella in vitro. J Mol Biol 1976;106:167–86.
[96] Kamiya R, Asakura S. Flagellar transformations at alkaline pH. J Mol Biol 1976;108:513–8.
[97] Matsuura S, Kamiya R, Asakura S. Transformation of straight flagella and recovery of motility in a mutant Escherichia coli. J Mol Biol 1978;118:431–40.
[98] Calladine CR. Design requirements for the construction of bacterial flagella. J Theor Biol 1976;57:469–89.
[99] Macnab RM, Ornston MK. Normal-to-curly flagellar transitions and their role in bacterial tumbling. Stabilization of an alternative quaternary structure by mechanical force. J Mol Biol 1977;112:1–30.
[100] Hotani H. Micro-video study of moving bacterial flagellar filaments. III. Cyclic transformation induced by mechanical force. J Mol Biol 1982;156:791–806.
[101] Darnton NC, Berg HC. Force-extension measurements on bacterial flagella: triggering polymorphic transformations. Biophys J 2007;92:2230–6.
[102] Wang X, Meng S, Han J. A continuum theoretical model and finite elements simulation of bacterial flagellar filament phase transition. J Biomech 2017;63:21–31.
[103] Calladine C. Construction and operation of bacterial flagella. Sci Prog 1983;68:365–85.
[104] Hasegawa K, Yamashita I, Namba K. Quasi- and nonequivalence in the structure of bacterial flagellar filament. Biophys J 1998;74:569–75.
[105] Goldstein RE, Goriely A, Huber G, Wolgemuth CW. Bistable helices. Phys Rev Lett 2000;84:1631–4.
[106] Coombs D, Huber G, Kessler JO, Goldstein RE. Periodic chirality transformations propagating on bacterial flagella. Phys Rev Lett 2002;89:118102.
[107] Srigiriraju SV, Powers TR. Continuum model for polymorphism of bacterial flagella. Phys Rev Lett 2005;94:248101.
[108] Srigiriraju SV, Powers TR. Model for polymorphic transitions in bacterial flagella. Phys Rev E 2006;73:011902.
[109] Speier C, Vogel R, Stark H. Modeling the bacterial flagellum by an elastic network of rigid bodies. Phys Biol 2011;8:046009.
[110] Vogel R, Stark H. Force-extension curves of bacterial flagella. Eur Phys J B 2010;33:259–71.
[111] Wada H, Netz RR. Discrete elastic model for stretching-induced flagellar polymorphs. Europhys Lett 2008;82:28001.
[112] Wang X, Sun Q. The mechanical phase transitions in biological systems. Adv Mech 2010;40:64–80.
[113] Wang XL, Sun QP. Mechanical analysis of phase transition experiments of the bacterial flagellar filament. Acta Mech Sin 2010;26:777–85.
[114] Wang X, Sun Q. Mechanical modeling of the bistable bacterial flagellar filament. Acta Mech Solida Sin 2011;24:1–16.
[115] Wang X, He Y, Sun Q. Simulation of bacterial flagellar phase transition by non-convex and non-local continuum modeling. Theor Appl Mech Lett 2011;1:044001.
[116] Wang X, Sun Q. Modeling of rate-dependent phase transition in bacterial flagellar filament. Mater Res Bull 2013;48:5019–25.
[117] Prokhnevsky A, Mamedov T, Leffet B, Rahimova R, Ghosh A, Mett V, et al. Developmental biology of the bacteria. Benjamin/Cummings Pub. Co.; 1985.
[118] Smits WK, Veening JW, Kuipers OP. Phenotypic variation and bistable switching in bacteria. Berlin, Heidelberg: Springer; 2008.
[119] Gustafsson A. Linnaeus' peloria: the history of a monster. Theor Appl Genet 1979;54:241–8.
[120] Stajic D, Bank C. Phenotypic switching and its evolutionary consequences. In: Phenotypic switching; 2020. p. 281–304.
[121] Ray J, Ewen AH, Prime CT. Ray's flora of Cambridgeshire = (Catalogus plantarum circa Cantabrigiam nascentium). Wheldon and Wesley; 1975.
[122] Mayr BE. The growth of biological thought: diversity, evolution, and inheritance. Harvard University Press; 1982.
[123] Darwin C. On the origin of the species. Graphic Arts Books; 2012.
[124] Mendel G. Experiments in plant hybridisation. Harvard University Press; 1950.
[125] Lenay C. Hugo De Vries: from the theory of intracellular pangenesis to the rediscovery of Mendel. C R Acad Sci, Sér 3 Sci Vie 2000;323:1053–60.
[126] Bradshaw AD. Evolutionary significance of phenotypic plasticity in plants. Adv Genet 1965;13:115–55.
[127] Nepal S, Kumar P. Dynamics of phenotypic switching of bacterial cells with temporal fluctuations in pressure. Phys Rev E 2018;97:052411.
[128] Evans TD, Zhang F. Bacterial metabolic heterogeneity: origins and applications in engineering and infectious disease. Curr Opin Biotechnol 2020;64:183–9.
[129] Waddington CH. The strategy of the genes. Routledge; 1957.
[130] Tadrowski AC, Evans MR, Bartlomiej W. Phenotypic switching can speed up microbial evolution. Sci Rep 2018;8:1–10.
[131] Desai SK, Kenney LJ. Switching lifestyles is an in vivo adaptive strategy of bacterial pathogens. Front Cell Infect Microbiol 2019;9:421.
[132] Bjarnsholt T. The role of bacterial biofilms in chronic infections. APMIS, Acta Pathol Microbiol Immunol Scand 2013;121:1–58.
[133] Costerton JW, Lewandowski Z, Caldwell DE, Korber DR, Lappinscott HM. Microbial biofilms. Annu Rev Microbiol 1995;49:711–45.
[134] Dunne Jr WM. Bacterial adhesion: seen any good biofilms lately? Clin Microbiol Rev 2002;15:155–66.
[135] Sousa A, Machado I, Pereira MO. Phenotypic switching: an opportunity to bacteria thrive. Formatex Research Center; 2011.
[136] Kirisits MJ, Prost L, Starkey M, Parsek MR. Characterization of colony morphology variants isolated from pseudomonas aeruginosa biofilms. Appl Environ Microbiol 2005;71:4809–21.
[137] Koh KS, Lam KW, Alhede M, Queck SY, Labbate M, Kjelleberg S, et al. Phenotypic diversification and adaptation of MG1 biofilm-derived morphotypes. J Bacteriol 2007;189:119–30.

[138] Jahn TL, Bovee EC. Movement and locomotion of microorganisms. Annu Rev Microbiol 1965;19:21–58.
[139] Kaiser D. Coupling cell movement to multicellular development in myxobacteria. Nat Rev Microbiol 2003;1:45–54.
[140] Koch AL. Unidirectional movement of flares of cells of myxococcus xanthus. Crit Rev Microbiol 2006;32:87–90.
[141] Mai-Prochnow A, Webb JS, Ferrari BC, Kjelleberg S. Ecological advantages of autolysis during the development and dispersal of pseudoalteromonas tunicata biofilms. Appl Environ Microbiol 2006;72:5414–20.
[142] Romanova YM, Smirnova TA, Andreev AL, et al. Formation of biofilms as an example of the social behavior of bacteria. Microbiology 2006;75:481–5.
[143] Chia N, Woese CR, Goldenfeld N. A collective mechanism for phase variation in biofilms. Proc Natl Acad Sci 2008;105:14597–602.
[144] Stewart PS, Franklin MJ. Physiological heterogeneity in biofilms. Nat Rev Microbiol 2008;6:199–210.
[145] Bookshelf N. A service of the National Library of Medicine, National Institutes of Health. Washington (DC): National Academies Press (US); 2010.
[146] Nguyen D, Singh PK. Evolving stealth: genetic adaptation of pseudomonas aeruginosa during cystic fibrosis infections. Proc Natl Acad Sci 2006;103:8305–6.
[147] Allegrucci M, Sauer K. Characterization of colony morphology variants isolated from streptococcus pneumoniae biofilms. J Bacteriol 2007;189:2030–8.
[148] Yildiz TH. Vibrio cholerae O1 El Tor: identification of a gene cluster required for the rugose colony type, exopolysaccharide production, chlorine resistance, and biofilm formation. Proc Natl Acad Sci 1999;96:4028–33.
[149] Boles BR, Thoendel M, Singh PK. Self-generated diversity produces "insurance effects" in biofilm communities. Proc Natl Acad Sci USA 2004;101:16630–5.
[150] Hansen SK, Rainey PB, Haagensen JA, Molin S. Evolution of species interactions in a biofilm community. Nature 2007;447:533–6.
[151] Baty AM, Eastburn CC, Diwu Z, Techkarnjanaruk S, Goodman AE, Geesey GG. Differentiation of chitinase-active and non-chitinase-active subpopulations of a marine bacterium during chitin degradation. Appl Environ Microbiol 2000;66:3566–73.
[152] Baty AM, Eastburn CC, Techkarnjanaruk S, Goodman AE, Geesey GG. Spatial and temporal variations in chitinolytic gene expression and bacterial biomass production. Appl Environ Microbiol 2000;66:3574–85.
[153] Keren I, Kaldalu N, Spoering A, Wang Y, Lewis K. Persister cells and tolerance to antimicrobials. FEMS Microbiol Lett 2004;230:13–8.
[154] Lewis K. Persister cells, dormancy and infectious disease. Nat Rev Microbiol 2007;5:48–56.
[155] Levin BR, Rozen DE. Non-inherited antibiotic resistance. Nat Rev Microbiol 2006;4:556–62.
[156] Balaban NQ, Merrin J, Chait R, Kowalik L, Leibler S. Bacterial persistence as a phenotypic switch. Science 2004;305:1622–5.
[157] Kussell E, Kishony R, Balaban NQ, Bacterial Leibler S. Persistence: a model of survival in changing environments. Genetics 2005;169:1807–14.
[158] Correia FF, D'Onofrio A, Rejtar T, et al. Kinase activity of overexpressed HipA is required for growth arrest and multidrug tolerance in escherichia coli. J Bacteriol 2006;188:8360–7.
[159] Korch SB, Hill TM. Ectopic overexpression of wild-type and mutant hipA genes in Escherichia coli: effects on macromolecular synthesis and persister formation. J Bacteriol 2006;188:3826–36.
[160] Li Y, Zhang Y. PhoU is a persistence switch involved in persister formation and tolerance to multiple antibiotics and stresses in Escherichia coli. Antimicrob Agents Chemother 2007;51:2092–9.
[161] Spoering AL, Vulic M, Lewis K. GlpD and PlsB participate in persister cell formation in Escherichia coli. J Bacteriol 2006;188:5136–44.
[162] Golden JW, Yoon HS. Heterocyst development in Anabaena. Curr Opin Microbiol 2003;6:557–63.
[163] Doherty GP, Bailey K, Lewis PJ. Stage-specific fluorescence intensity of GFP and mCherry during sporulation. In: Bacillus subtilis. BMC research notes, vol. 3. 2010. p. 1–8.
[164] Swain MR, Ray RC. Biocontrol and other beneficial activities of Bacillus subtilis isolated from cowdung microflora. Microbiol Res 2009;164:121–30.
[165] Kearns DB, Losick R. Cell population heterogeneity during growth of Bacillus subtilis. Genes Dev 2005;19:3083–94.
[166] Branda SS, Gonzalez-Pastor JE, Ben-Yehuda S, Losick R, Kolter R. Fruiting body formation by Bacillus subtilis. Proc Natl Acad Sci USA 2001;98:11621–6.
[167] Rudner DZ, Losick R. Morphological coupling in development. Dev Cell 2001;1:733–42.
[168] Hilbert P. Sporulation of Bacillus subtilis. Curr Opin Microbiol 2004;7:579–86.
[169] Curtis PD, Taylor RG, Welch RD, Shimkets LJ. Spatial organization of myxococcus xanthus during fruiting body formation. J Bacteriol 2007;189:9126–30.
[170] Dubnau D. Genetic competence in Bacillus subtilis. Microbiol Rev 1991;55:395–424.
[171] Dubnau D, Provvedi R. Internalizing DNA. Res Microbiol 2000;151:475–80.
[172] González-Pastor JE, Hobbs EC, Losick R. Cannibalism by sporulating bacteria. Science 2003;301:510–3.
[173] Mazza P. The use of Bacillus subtilis as an antidiarrhoeal microorganism. Boll Chim Farm 1994;133:3–18.
[174] Evdokimov AG, Pokross ME, Egorov NS, Zaraisky AG, Yampolsky IV, Merzlyak EM, et al. Structural basis for the fast maturation of Arthropoda green fluorescent protein. EMBO Rep 2006;7:1006–12.
[175] Falk MM, Baker SM, Gumpert AM, Segretain D, Buckheit RW. Gap junction turnover is achieved by the internalization of small endocytic double-membrane vesicles. Mol Biol Cell 2009;20:3342–52.
[176] Chudakov DM, Matz MV, Lukyanov S, Lukyanov KA. Fluorescent proteins and their applications in imaging living cells and tissues. Physiol Rev 2010;90:1103–63.
[177] Verplaetse E, Slamti L, Gohar M, et al. Cell differentiation in a bacillus thuringiensis population during planktonic growth, biofilm formation, and host infection. mBio 2015;6:00138.
[178] Seminara A, Angelini TE, Wilking JN, Vlamakis H, Ebrahim S, Kolter R, et al. Osmotic spreading of Bacillus subtilis biofilms driven by an extracellular matrix. Proc Natl Acad Sci USA 2012;109:1116–21.

[179] O'Toole G, Kaplan HB, Kolter R. Biofilm formation as microbial development. Annu Rev Microbiol 2000;54:49–79.
[180] Chang S, Cohen SN. High frequency transformation of Bacillus subtilis protoplasts by plasmid DNA. Mol Gen Genet 1979;168:111–5.
[181] Wang X, Koehler SA, Wilking JN, Sinha NN, Cabeen MT, Srinivasan S, et al. Probing phenotypic growth in expanding Bacillus subtilis biofilms. Appl Microbiol Biotechnol 2016;100:4607–15.
[182] Hendricks TR, Lee I. Wrinkle-free nanomechanical film: control and prevention of polymer film buckling. Nano Lett 2007;7:372–9.
[183] Harrison C, Stafford CM, Zhang W, Karim A. Sinusoidal phase grating created by a tunably buckled surface. Appl Phys Lett 2004;85:4016–8.
[184] Pretzl M, Schweikart A, Hanske C, Chiche A, Fery A. A lithography-free pathway for chemical microstructuring of macromolecules from aqueous solution based on wrinkling. Langmuir 2008;24:12748–53.
[185] Jiang X, Takayama S, Qian X, Ostuni E, Wu H, Bowden N, et al. Controlling mammalian cell spreading and cytoskeletal arrangement with conveniently fabricated continuous wavy features on poly(dimethylsiloxane). Langmuir 2002;18:3273–80.
[186] Teixeira AI, Abrams GA, Bertics PJ, Murphy CJ, Nealey PF. Epithelial contact guidance on well-defined micro- and nanostructured substrates. J Cell Sci 2003;116:1881–92.
[187] Uttayarat P, Toworfe G, Dietrich F, Lelkes P. Topographic guidance of endothelial cells on silicone surfaces with micro- to nanogrooves: orientation of actin filaments and focal adhesions. J Biomed Mater Res, Part A 2005;75:668–80.
[188] Guo C, Feng Y, Zhai J, Wang G, Song Y, Jiang L, et al. Large-area fabrication of a nanostructure-induced hydrophobic surface from a hydrophilic polymer. ChemPhysChem 2004;5:750–3.
[189] Okegbe C, Price-Whelan A, Dietrich LE. Redox-driven regulation of microbial community morphogenesis. Curr Opin Microbiol 2014;18:39–45.
[190] Kayser J, Schreck CF, Yu Q, Gralka M, Hallatschek O. Emergence of evolutionary driving forces in pattern-forming microbial populations. Philos Trans R Soc B, Biol Sci 2018;373:20170106.
[191] Cheng Z, Li B, Huang X, Yong N, Feng XQ. Morphomechanics of bacterial biofilms undergoing anisotropic differential growth. Appl Phys Lett 2016;109:143701.
[192] Giverso C, Verani M, Ciarletta P. Branching instability in expanding bacterial colonies. J R Soc Interface 2015;12:20141290.
[193] Wilking JN, Zaburdaev V, De Volder M, et al. Liquid transport facilitated by channels in Bacillus subtilis biofilms. Proc Natl Acad Sci 2012;110:848–52.
[194] Aguilar C, Eichwald C, Eberl L. Multicellularity in bacteria: from division of labor to biofilm formation. In: Evolutionary transitions to multicellular life; 2015. p. 79–95.
[195] Cheng Z, Li B, Tang JY, Wang XL, Qin Z, Feng XQ. Experimental and theoretical studies on the morphogenesis of bacterial biofilms. Soft Matter 2017;13:7389–97.
[196] Kato T, Hatori J, Yoshida Y, Matsuo Y, Ikehata S. Irreversible phase transition and spontaneous strain in CsHSO4. Solid State Ion 2007;178:735–9.
[197] Yurasov N, Yurasova I, Plokhikh A, Galkin N, Tetyanchuk V, Dolgikh E. Irreversible phase transitions in structural elements of synthetic opal. J Phys Conf Ser 2019:012082.
[198] Seara DS, Machta BB, Murrell MP. Irreversibility in dynamical phases and transitions. Nat Commun 2021;12:1–9.
[199] Fruchart M, Hanai R, Littlewood PB, Vitelli V. Non-reciprocal phase transitions. Nature 2021;592:363–9.
[200] Xiong L, Cao Y, Cooper R, Rappel WJ, Tsimring L. Flower-like patterns in multi-species bacterial colonies. eLife 2020;9:e48885.
[201] Yan J, Fei C, Mao S, Moreau A, Bassler BL. Mechanical instability and interfacial energy drive biofilm morphogenesis. eLife 2019;8:e43920.
[202] Asally M, Kittisopikul M, Rue P, Du Y, Hu Z, Cagatay T, et al. Localized cell death focuses mechanical forces during 3D patterning in a biofilm. Proc Natl Acad Sci 2012;109:18891–6.
[203] Wang X, Tan Y, Liu J, Hu S, Zhao H. The evolving wrinkle pattern of the Bacillus subtilis biofilm providing more living space for cells. J Mech Med Biol 2020;20:2050048.
[204] Ball RC, Brady RM, Rossi G, Thompson BR. Anisotropy and cluster growth by diffusion-limited aggregation. Phys Rev Lett 1985;55:1406–9.
[205] Meakin P. Formation of fractal clusters and networks by irreversible diffusion-limited aggregation. Phys Rev Lett 1983;51:1119–22.
[206] Halsey TC. Diffusion-limited aggregation: a model for pattern formation. Phys Today 2000;53:36–41.
[207] Amar MB, Goriely A. Growth and instability in elastic tissues. J Mech Phys Solids 2005;53:2284–319.
[208] Glenny RW, Robertson HT. Fractal modeling of pulmonary blood flow heterogeneity. J Appl Physiol 1991;70:1024–30.
[209] Caruthers SD, Harris TR. Effects of pulmonary blood flow on the fractal nature of flow heterogeneity in sheep lungs. J Appl Physiol 1994;77:1474–9.
[210] Ben-Jacob E, Garik P. The formation of patterns in non-equilibrium growth. Nature 1990;343:523–30.
[211] Vicsek T, Zafeiris A. Collective motion. Phys Rep 2012;517:71–140.
[212] Marcos, Fu HC, Powers TR, Stocker R. Bacterial rheotaxis. Proc Natl Acad Sci USA 2012;109:4780–5.
[213] Lopez D, Vlamakis H, Kolter R. Generation of multiple cell types in Bacillus subtilis. FEMS Microbiol Rev 2008;33:152–63.
[214] Lehn JM. Toward self-organization and complex matter. Science 2002;295:2400–3.
[215] Vicsek T, Cserző M, Horváth VK. Self-affine growth of bacterial colonies. Physica A 1990;167:315–21.
[216] Vicsek T, Czirók A, Ben-Jacob E, et al. Novel type of phase transition in a system of self-driven particles. Phys Rev Lett 1995;75:1226–9.
[217] Mitchell M. A guided tour. Oxford University Press; 2009.
[218] Paton R, Bolouri H, Holcombe W, Parish JH, Tateson R. Computation in cells and tissues. Springer; 2004.
[219] Benjacob E. Bacterial self-organization: co-enhancement of complexification and adaptability in a dynamic environment. Philos Trans R Soc, Math Phys Eng Sci 2003;361:1283–312.
[220] Ricardo MG, Nadell CD, Raimo H, Knut D, Bonachela JA, Igoshin OA. Cell adhesion and fluid flow jointly initiate genotype spatial distribution in biofilms. PLoS Comput Biol 2018;14:e1006094.

[221] Momeni B. Division of labor: how microbes split their responsibility. Curr Biol 2018;28:697–9.
[222] Dervaux J, Magniez JC, Libchaber A. On growth and form of Bacillus subtilis biofilms. Interface Focus 2014;4:20130051.
[223] Mimura M, Sakaguchi H, Matsushita M. Reaction–diffusion modelling of bacterial colony patterns. Physica A 2000;282:283–303.
[224] Hu S, Wang X, Tan Y, Liu J, Zhao H. 'Chain and running' induced by mechanical interactions among cells of different phenotypes in the Bacillus subtilis biofilm. Eur Biophys J 2021;50:1013–23.
[225] Matsuzaki M, Kikura H, Matsushita J, Masanori Aritomi HA. Real-time observation of Brownian motion and cluster movement of ferro- and non-magnetic particles in magnetic fluids. Sci Technol Adv Mater 2004;5:667–71.
[226] Wolfram S. Cellular automata and complexity. CRC Press; 2008.
[227] Olfati-Saber R. Flocking for multi-agent dynamic systems: algorithms and theory. IEEE Trans Autom Control 2006;51:401–20.
[228] Reynolds CW. Flocks, herds and schools: a distributed behavioral model. In: Proceedings of the 14th annual conference on computer graphics and interactive techniques; 1987.
[229] Pérez-Velázquez J, Gölgeli M, García-Contreras R. Mathematical modelling of bacterial quorum sensing: a review. Bull Math Biol 2016;78:1585–639.
[230] Dunham S, Ellis JF, Li B, Ee Dler Sw, Mass JV. Spectrometry imaging of complex microbial communities. Acc Chem Res 2017;50:96–104.
[231] Bridier A, Coq DL, Dubois-Brissonnet F, Thomas V, Aymerich S, Briandet R. The spatial architecture of Bacillus subtilis biofilms deciphered using a surface-associated model and situ imaging. PLoS ONE 2011;6:e16177.
[232] Kumar S. Order parameter in bacterial biofilm adaptive response. Front Microbiol 2018;9:01721.
[233] Bak P, Chao T, Wiesenfeld K. Self-organized criticality: an explanation of the 1/f noise. Phys Rev Lett 1987;59:381–4.
[234] Roy S, Chen YL. Rich phase transitions in strongly confined polymer–nanoparticle mixtures: nematic ordering, crystallization, and liquid–liquid phase separation. J Chem Phys 2021;154:024901.
[235] Hesse J, Gross T. Self-organized criticality as a fundamental property of neural systems. Front Syst Neurosci 2014;8:00166.
[236] Selvarajoo K. Large scale-free network organization is likely key for biofilm phase transition. Eng Biol 2019;3:67–71.
[237] Blumenfeld R. Isostaticity and controlled force transmission in the cytoskeleton: a model awaiting experimental evidence. Biophys J 2006;91:1970–83.
[238] You Z, Pearce D, Sengupta A, Giomi L. Mono-to-multilayer transition in growing bacterial colonies. Phys Rev Lett 2019;123:178001.
[239] Wang X, Shen X, Wang Z, Kong Y. Viscoelasticity variation in a biofilm-mediated Bacillus subtilis suspension induced by adding polyethylene glycol. Eur Biophys J 2019;48:599–608.
[240] Dohnt K, Sauer M, Müller M, Atallah K, Weidemann M, Gronemeyer P, et al. An in vitro urinary tract catheter system to investigate biofilm development in catheter-associated urinary tract infections. J Microbiol Methods 2011;87:302–8.
[241] Dorken G, Ferguson GP, French CE, Poon W. Aggregation by depletion attraction in cultures of bacteria producing exopolysaccharide. J R Soc Interface 2012;9:3490–502.
[242] Drescher K, Shen Y, Bassler BL, Stone HA. Biofilm streamers cause catastrophic disruption of flow with consequences for environmental and medical systems. Proc Natl Acad Sci 2013;110:4345–50.
[243] Eboigbodin KE, Newton JRA, Routh AF, Biggs CA. Role of nonadsorbing polymers in bacterial aggregation. Langmuir 2005;21:12315–9.
[244] Ghosh P, Mondal J, Ben-Jacob E, Levine H. Pattern formation in a growing bacterial colony facilitated by extra-cellular polymeric substances; 2015.
[245] Dewangan NK, Tran N, Wang-Reed J, Conrad JC. Bacterial aggregation assisted by anionic surfactant and calcium ions. Soft Matter 2021;17:8474–82.
[246] Steinhardt PJ, Nelson DR, Ronchetti M. Bond-orientational order in liquids and glasses. Phys Rev B 1983;28:784–805.
[247] Ghosh P, Mondal J, Ben-Jacob E, Levine H. Mechanically-driven phase separation in a growing bacterial colony. Proc Natl Acad Sci 2015;112:2166–73.
[248] Zhai X, Larkin JW, Kikuchi K, Redford SE, Mugler A. Statistics of correlated percolation in a bacterial community. PLoS Comput Biol 2019;15:e1007508.
[249] Stauffer D, Aharony A. Introduction to percolation theory. Taylor & Francis; 2018.
[250] Dell'Arciprete D, Blow ML, Brown AT, Farrell F, Lintuvuori JS, Mcvey AF, et al. A growing bacterial colony in two dimensions as an active nematic. Nat Commun 2018;9:1–9.
[251] Hartmann R, Singh PK, Pearce P, Mok R, Song B, Díaz-Pascual F, et al. Emergence of three-dimensional order and structure in growing biofilms. Nat Phys 2019;15:251–6.